COASTAL RESEARCH AND EDUCATION ACTIONS FOR TRANSPORTATION EQUITY
TIER 1 UNIVERSITY TRANSPORTATION CENTER
U.S. DEPARTMENT OF TRANSPORTATION

SEAHIVE® solutions to mitigate bridge scour – Phase II

October 14, 2025

Nanni, Antonio, Ph.D., P.E., Professor at University of Miami, Department of Civil & Architectural Engineering, 1251 Memorial Drive, McArthur Engineering Building, FL 33146; ORCID https://orcid.org/0000-0003-2678-9268; Email: nanni@miami.edu
Barbarigos, Landolf, Ph.D., Associate Professor at University of Miami, 1251 Memorial Drive, McArthur Engineering Building, FL 33146; ORCID https://orcid.org/0000-0001-7550-800X; Email: landolfrb@miami.edu

Kulesza, Stacey, Ph.D., P.E., Associate Professor at Texas State University, Ingram School of Engineering, 327 W Woods St, San Marcos, TX 78666; ORCID https://orcid.org/0000-0000-0000-0000; Email: sekulesza@txstate.edu

Heydarpour, Khashayar, Ph.D. Student at University of Miami, Department of Civil & Architectural Engineering, 1251 Memorial Drive, McArthur Engineering Building, FL 33146 Email: kxh852@miami.edu

Enayati Shabkolaei, Mohammad, Ph.D. Student at University of Miami, Department of Civil & Architectural Engineering, 1251 Memorial Drive, McArthur Engineering Building, FL 33146 Email: mxe938@miami.edu

Farghal, Husam Mohammed Ali, Ph.D. Student at University of Miami, Department of Civil & Architectural Engineering, 1251 Memorial Drive, McArthur Engineering Building, FL 33146 Email: hxf350@miami.edu

Annual Research Report – Part II

Prepared for:

Coastal Research and Education Actions for Transportation Equity

Technical Report Documentation Form

1. Report No. 2301-3	2. Government Accession No. 01929243	3. Recipient's Catalog No. n/a
4. Title and Subtitle SEAHIVE® solutions to mitigate bridge scour – Phase II		5. Report Date 10/15/2025
7. Author(s) Antonio Naznni, nanni@miami.edu, 305-284-3461, 0000-0003-2678-9268, University of Miami; Landolf Barbarigos, ladolfrb@miami.edu, 305-284-3489, 0000-0001-7550-800X, University of Miami		6. Performing Organization Code n/a
9. Performing Organization Name and Address University of Miami, Dept of Civil & Architectural Eng. College of Engineering, 1251 Memorial Dr. Coral Gables, FL 33145		8. Performing Organization Report No. n/a 10. Work Unit No. (TRAIS) n/a
12. Sponsoring Agency Name and Address Office of the Assistant Secretary for Research and Technology University Transportation Centers Program Department of Transportation Washington, DC United States 20590		11. Contract or Grant No. 69A3552348330 13. Type of Report and Period Covered Final Project Report 6/01/2024-05/31/2025
15. Supplementary Notes		14. Sponsoring Agency Code OST-R
https://create.engineering.txst.edu/		

16. Abstract

This study investigates the structural performance of internally prestressed concrete (PC) SEAHIVE® units as part of an ongoing effort to mitigate bridge scour and improve coastal resilience with green-gray technologies. Unlike Phase I of this research, which focused on wet-cast and externally wrapped dry-cast concrete SEAHIVE® units tested under pure compression and four-point bending, the present work introduces internal pre-tensioned GFRP reinforcement to improve mechanical characteristics and serviceability by delaying crack formation and decreasing their width. PC SEAHIVE® units were designed and fabricated with six GFRP bars to provide adequate prestress. The experimental program comprised standardized material characterization and full-size structural testing, including four-point bending of perforated SEAHIVE® elements. Results demonstrated that pretensioning effectively increased the cracking load, delayed diagonal cracking, and reduced crack widths, particularly at midspan where prestress transfer was fully developed. Finite element simulations using Abaqus Concrete Damaged Plasticity (CDP) models further validated the observed behaviors and were able to capture flexure–shear cracking patterns while highlighting the influence of perforations.

17. Key Words Prestressed concrete; GFRP reinforcement; Hollow concrete shape; Flexural capacity		18. Distribution Statement No Restrictions	
19. Security Classification (of this report) Unclassified	20. Security Classification (of this page) Unclassified	21. No. of Pages 48	22. Price n/a

ACKNOWLEDGMENT

This study was funded, partially or entirely, by the U.S. Department of Transportation through the Coastal Research and Education Actions for Transportation Equity University Transportation Center under Grant Award Number 69A3552348330. The work was conducted at the University of Miami.

DISCLAIMER

ABSTRACT

This study investigates the structural performance of internally prestressed concrete (PC) SEAHIVE® units as part of an ongoing effort to mitigate bridge scour and improve coastal resilience with green-gray technologies. Unlike Phase I of this research, which focused on wet-cast and externally wrapped dry-cast concrete SEAHIVE® units tested under pure compression and four-point bending, the present work introduces internal pre-tensioned GFRP reinforcement to improve mechanical characteristics and serviceability by delaying crack formation and decreasing their width. PC SEAHIVE® units were designed and fabricated with six GFRP bars to provide adequate prestress. The experimental program comprised standardized material characterization and full-size structural testing, including four-point bending of perforated SEAHIVE® elements. Results demonstrated that pretensioning effectively increased the cracking load, delayed diagonal cracking, and reduced crack widths, particularly at midspan where prestress transfer was fully developed. Finite element simulations using Abaqus Concrete Damaged Plasticity (CDP) models further validated the observed behaviors and were able to capture flexure–shear cracking patterns while highlighting the influence of perforations.

Keywords: Prestressed concrete; GFRP reinforcement; Hollow concrete shape; Flexural capacity

Table of Contents

List of Figures

List of Tables

INTRODUCTION

According to the data published by National Oceanic and Atmospheric Administration (NOAA), Approximately 40% of the U.S. population resides in coastal counties, and the Southeast alone encompasses over 70 million people along 29,000 miles of coastline [1]. These communities face increasing vulnerability to hurricanes and storm surges. In the last four decades, U.S. weather-related disasters have inflicted over $2 trillion in damages [2]. Prominent recent events such as Hurricanes *Ian* (2022) and *Michael* (2018) underscore a critical need for effective and cost-efficient measures to protect coastal infrastructure and communities [3], [4], [5].

As discussed in the previous study [6], conventional shoreline protection strategies, including rubble mound revetments and vertical seawalls, have notable limitations. The primary objective of traditional seawalls is to reflect incident wave energy rather than dissipating it, that often results in exacerbating local scour and beach erosion due to reflected turbulence [7]. Moreover, poor ecological outcomes resulted from such structures. For instance, vertical seawalls typically support almost 23% lower biodiversity and 45% fewer organisms relative to natural shorelines [8]. As the consequence of this gap a broad research regarding eco-friendly coastal defense and innovative “green-gray” infrastructure that combines the robustness of engineered structures with improved energy dissipation and habitat features has initiated.

One such innovation is the SEAHIVE® technology known as a modular system of perforated hexagonal concrete units designed to dissipate wave energy and reduce scour. For example, Figure 1 shows an assemblage of six of these units plus two solid half-units that could be used for a submerged or partially-submerged reef. Ghiasian et al. [9] introduced SEAHIVE® as interlocking hollow hexagonal prisms that resemble a honeycomb, constructed of reinforced concrete (RC) with strategically placed voids and openings on their faces. These voids allow incident waves to pass through the structure and break up wave force. SEAHIVE® encourages internal turbulence that dissipates energy, rather than reflecting it seaward. Experiments have shown this hollow hexagon system can significantly attenuate waves. In the meanwhile, interstitial spaces are provided as a space for hospitable marine life, an ecological advantage over solid seawalls [7]. In effect, SEAHIVE® units function similarly to known porous coastal defenses such as Tetrapods, X-blocs, reef balls in breaking wave momentum and promoting sediment deposition, but their stackable, interlocking geometry offers improved stability and versatility.

Figure 1: Manufactured SEAHIVE® units

Beyond coastal wave attenuation, SEAHIVE® technology has shown promising performance in mitigating hydraulic scour at bridge supports and waterfront structures. Scour, the erosion of soil around foundations due to flowing water, is a leading cause of bridge failures, implicated in approximately 66% of bridge collapses in North America and Europe [10] and about 20% of U.S. bridge failures [8], [11], [12]. Horseshoe vortices at the base of bridge pier or abutment are attributed to fast-moving water that remove sediment and can undermine the foundation. To resolve this problem countermeasures like riprap and loose rock are suggested, however, they can be dislodged or prove insufficient during major floods. SEAHIVE® units offer a novel countermeasure by encircling a pier or lining a channel bed with these perforated concrete hex-tubes, the flow is disrupted and redirected through the unit voids, resulting in the intensity of erosive vortices reduction. Preliminary concepts propose wrapping bridge piers with a SEAHIVE® array to alter flow patterns around the pile cap and between closely spaced piles, thereby addressing both local and contraction scour mechanisms [9]. In essence, the geometry of SEAHIVE® originally aimed at mitigating waves can also calm aggressive currents around structures.

Although the hydrodynamic benefits of SEAHIVE® have been demonstrated in laboratory and field pilots, its structural performance under service and extreme loads remains an open question. The unique configuration of SEAHIVE® units including a hexagonal cross-section that is hollow and perforated introduces a complex load path and stress distribution unlike conventional solid members. Expanded evaluation of their structural capacity and failure modes is needed before widespread deployment**.** To date, most relevant design guidance is extrapolated from studies on reinforced concrete beams with web openings or perforated solid sections [13], [14], [15], [16], [17], [18], [19] which indicate that introducing openings can significantly reduce flexural stiffness and strength if not properly reinforced. With all the widespread studies on planar beams, comparable data on perforated hollow hexagonal units is scarce. Key questions include how the voids and thin web sections affect the unit's compression capacity, shear resistance (especially at the interlocking joints), and fatigue performance under wave cyclic loading. Furthermore, different fabrication methods may lead to different material properties and structural behavior. SEAHIVE® modules can be manufactured via at least three methods: wet-cast concrete, dry-cast concrete, or 3D printing. *Wet-cast* (conventional cast-in-form casting) allows complex reinforcement layouts but is labor-intensive for large production runs.

To maximize the structural capacity and durability of SEAHIVE® elements, the use of prestressed concrete (PC) and non-corrosive reinforcement is being explored. Prestressed concrete – wherein high-strength steel strands or FRP bars induce compressive pre-stress in the member – offers well-known advantages for structural applications. By pre-compressing the concrete, tensile cracking under service loads is delayed or minimized, leading to higher fatigue life and improved durability in aggressive environments. Prestressing also enables longer spans or larger modular units by effectively increasing the member's stiffness and load capacity, all within serviceability limits set by design codes (e.g., crack width and deflection limits in *ACI 318-19* [20, p. 318] for structural concrete). In the context of SEAHIVE®, a prestressed *hex-tube* unit could resist greater wave impacts or earth pressures (when used in a retaining wall configuration) than a non-prestressed unit of the same size. For example, Florida DOT's developmental design for a SEAHIVE®-based sheet pile seawall envisions hexagonal modules up to 9 m (30 ft) long – a dimension readily achievable with precast prestressed construction – to meet the flexural and shear demands of a cantilevered wall. By employing precast, pretensioned concrete fabrication, multiple SEAHIVE® units can be produced with uniform quality and then keyed together during installation, forming a continuous protective barrier.

A critical innovation under review is the integration of fiber-reinforced polymer (FRP) reinforcement in lieu of conventional steel, especially for marine exposure. GFRP (glass FRP) bars and CFRP strands offer corrosion immunity in saltwater and high chloride environments, addressing the well-documented deterioration of steel-reinforced marine structures due to corrosion [21], [22]. However, FRP materials differ fundamentally from steel in their behavior: they are linear elastic to failure (no yield plateau) and generally have lower elastic modulus. Design guides such as *ACI 440.1R-15* [23] and standards such as *CSA S806-12* [24] recognize these differences and specify appropriate reduction factors and design criteria for FRP-reinforced concrete. For instance, CSA S806-12 limits the allowable stress in FRP tension ties (via a φ-factor of 0.65 for bonded FRP) [24], reflecting the need for a conservative design due to FRP's lack of ductility. In prestressing applications, GFRP and basalt FRP (BFRP) bars are typically stressed to only about 30% of the ultimate tensile strength (compared to ~70–80% for steel strand) to avoid creep rupture [23], [24]. Research has demonstrated that with the use of GFRP bars in a prestressed scheme, flexural capacity and stiffness of the member enhances significantly while crack widths are kept small [25]. The absence of steel eliminates the risk of corrosion, considered as a paramount concern for offshore infrastructure that is in contact with seawater. Recent projects such as GFRP-reinforced concrete seawall in Miami [21], and permeable FRP-reinforced caissons for wave attenuation [26], have validated the constructability of FRP-reinforced and FRP-prestressed coastal elements

In the previous project phase (Annual Report Part 1, 2024), wet-cast and dry-cast SEAHIVE® elements were investigated under pure compression and four-point bending to establish a structural baseline. The SEAHIVE® units in that study were reinforced either with internal GFRP bars or external GFRP wraps. Key findings from Phase I indicated that under axial compression the thin hexagonal legs cracked once the concrete's tensile capacity was exceeded, that resulted in the failure of both internally reinforced and externally wrapped units. In flexural testing, the internally GFRP-reinforced beams failed due to insufficient development length of the longitudinal bars coupled with concrete toe crushing at the supports. The GFRP-wrapped specimen demonstrated a different limitation where debonding and slippage of the longitudinal FRP strips initiated flexural cracking. These results highlighted that while the dry-cast, GFRP-reinforced SEAHIVE® concept was structurally viable, its capacity was limited by reinforcement detailing and concrete tensile strength. Notably, the externally applied, pretensioned GFRP wrapping showed promise in confining the structure and delaying catastrophic failure. This validated the SEAHIVE® concept as a feasible scour and wave mitigation unit, but also underscored the need for design enhancements – particularly to address tensile cracking and flexural performance – as the project moved forward. Based on the obtained information from Phase I, and the observed limitations, the motivation to pursue a new approach in the current study is to focus on prestressing and material improvements to achieve higher strength and more resilient SEAHIVE® units.

Building on Phase I findings, this report (Annual Report Phase II, 2025) introduces structural innovations centered on prestressed concrete (PC) SEAHIVE® units. Prestressing is implemented here by pretensioning six internal GFRP bars within the hexagonal modules prior to concrete casting. By inducing compressive pre-stress, the formation of tensile cracks under service loads is delayed, stiffness increases, and the durability in aggressive environments is improved. These benefits are especially essential for SEAHIVE® units, which must endure repetitive wave loading and impact while limiting crack widths to protect long-term integrity. Prestressing also enables greater load capacity and permits longer modular units without sacrificing serviceability. For example, a recent FDOT conceptual design for a SEAHIVE®-based seawall envisions hexagonal precast modules up to 9 m (30 ft) long. This span is feasible only through precast pretensioned construction.

A critical aspect of this Phase II study is the use of pre-stressed GFRP bars. The PC SEAHIVE® units employ high-strength GFRP bars as internal reinforcement. GFRP differs from steel in mechanical behavior as it is linear elastic to failure and has a lower elastic modulus. Design standards such as ACI 440.11-22 [27] and CSA S806 [24] account for these differences by prescribing conservative reduction factors and strain limits for FRP-reinforced concrete to ensure safe performance. For instance, CSA S806-12 [24] limits the usable stress in FRP tension reinforcement to mitigate the lack of ductility. In prestressed applications, FRP bars are typically jacked to a lower initial stress level relative to steel to avoid creep rupture.

In summary, the present study diverges from and advances beyond Phase I work. A transition from examining non-prestressed, conventionally reinforced SEAHIVE® modules to developing a prestressed, GFRP-reinforced system with superior performance and durability is exhibited. The incorporation of prestressing and high-strength materials is aimed at overcoming the limitations identified in Phase I such as tensile cracking and limited flexural capacity. The subsequent sections of this report provide a detailed account of prototype fabrication, experimental results, and analytical evaluations for the PC SEAHIVE® units. Through this research, it is aimed to establish design criteria and recommendations that enable transportation agencies (DOTs) to confidently deploy SEAHIVE® units as part of a multi-hazard coastal defense and bridge scour protection strategy. The innovations documented herein represent a significant step toward making SEAHIVE® a practical and reliable solution for protecting coastal transportation infrastructure against wave impact and scour.

FABRICATION PROCESS OF PRESTRESSED SEAHIVE® MODULES

The construction of prestressed SEAHIVE® modules begins with the careful setup of specialized molds, as depicted in Figure 2, showing a stack of conical steel elements intended to allow discontinuities on the hexagon surface. These cones are strategically positioned within a larger hexagonal mold frame to create perforations essential to the SEAHIVE® system's functionality. The conical design with varying diameters for inner and outer holes facilitates demolding during construction and allows for wave energy dissipation and habitats for marine life during service. Precision in mold assembly is critical, supporting the module's ability to withstand wave and current forces while offering ecological benefits.

Figure 2: Stack of steel cones for perforating SEAHIVE® prestressed modules (Patent pending filed by SIGMAc s.r.l., Vicenza, Italy).

Considering the 790 mm height of the SEAHIVE® modules, which generate significant hydrostatic pressure from fresh concrete in the lower regions, steel molds are employed for specimen fabrication to ensure structural stability and prevent bulging and deformation, as illustrated in Figure 3. Finally, Figure 4 shows the fabrication setup of the prestressed SEAHIVE® modules after completion of the mold, which define the hollow sections and ensure the required geometry during casting. Also visible in this photograph is a GFRP bar ready for tensioning.

Figure 3: Fabrication of steel molds for SEAHIVE® modules (Patent pending filed by SIGMAc s.r.l., Vicenza, Italy).

Figure 4: Completed mold (Patent pending filed by SIGMAc s.r.l., Vicenza, Italy).

After installing the anchoring components on both ends of the GFRP bars, the prestressing process is carried out, during which the GFRP bars are pulled using a specialized jack from one side. The end where the pulling occurs is referred to as the live end, while the opposite end is called the dead end. According to the design, all six GFRP bars were tensioned to forces ranging from 27 to 41 tons to achieve stresses between 240 and 363 MPa, depending on the specimen. Once the specified tension is reached, the jack is deactivated, releasing the GFRP bars. At this point, the anchoring components maintain the bars in their tensioned state, ensuring that the applied force is preserved (Figure 5.)

Figure 5: Prestressing of GFRP bars in SEAHIVE® module fabrication (Patent pending filed by SIGMAc s.r.l., Vicenza, Italy).

The setup maintains stability, allowing the concrete to cure while integrating the prestressed reinforcements effectively (Figure 6).

Figure 6: Final prestressed GFRP SEAHIVE® module in the conical steel mold after concrete casting (Patent pending filed by SIGMAc s.r.l., Vicenza, Italy).

A set of cubes was prepared for each SEAHIVE® cast to assess concrete mechanical properties. Three 150 x 150 mm cubes were made per SEAHIVE® following EN 12390-3 [28]. All produced cubes, to be crushed at the time of each SEAHIVE® testing are shown in Figure 7.

Figure 7: Fabrication of cubic samples during SEAHIVE® specimens casting.

As presented in Figure 8, Twenty-four hours after concrete casting, the molds were opened. During demolding, the module is separated from the steel frame using controlled force to ensure the structural integrity of the prestressed GFRP-reinforced concrete is maintained. The GFRP bars were cut with an abrasive disc one by one in this sequence: three bars on one side, then all six bars on the opposite side, and, finally, the last three bars on the first side. The process requires active monitoring to prevent damage to the perforations or the module's geometry, which are critical for its functionality.

Figure 8: Demolding of SEAHIVE® module with lifting equipment (Patent pending filed by SIGMAc s.r.l., Vicenza, Italy)

All cubic specimens and fabricated SEAHIVE® modules were subjected to a curing process to ensure optimal strength development. A subset of the cubic specimens was tested for compressive strength at regular intervals during the initial curing phase to monitor the progression of concrete compressive strength. Upon confirmation that the compressive strength had reached a minimum threshold of 42 MPa—indicative of sufficient structural integrity—the initial curing process was discontinued. Subsequently, the release of the prestressing force within the GFRP-reinforced specimens was initiated.

Unlike steel, FRP materials are linear elastic to failure and no yielding plateau is exhibited. Consequently, prestressing levels must be restricted to about 30-40% of the design tensile strength (compared to 70–80% for steel) to prevent creep rupture and excessive relaxation losses [29]. Furthermore, brittleness requires careful stress control during jacking operations, as overstressing can cause sudden failure.

From a practical standpoint, fabrication and handling challenges exist in GFRP bars. Solid GFRP bars cannot be easily coiled like steel strands, which limits transport length to around 12 meters for bars with diameter larger than 12 mm, while bars of smaller diameter can be coiled on reels that are less than 2 meters tall. Bar anchorage for pretensioning is also difficult because conventional wedge systems used for steel strands may crush the bar due the fact that transverse compressive strength is resin dominated.

PRESTRESSED UNITS REINFORCED INTERNALLY WITH GFRP BARS

Test Specimens

To evaluate the capacity of PC SEAHIVE®, eight specimens were fabricated and seven of them subjected to four-point flexural loading. The manufacturer produced eight PC SEAHIVE® units. Table 1 provides a comprehensive overview of all tested specimens. Data for specimen 18 (D2) is not included in this report, as this specimen requires FRP wrapping at its ends prior to testing.

Specimen fabrication

Prestressing forces were applied to the six GFRP bars utilizing MIBA hydraulic jacks. These jacks are capable of delivering prestressing loads of 6, 10, and 30 tons (approximately 60, 100, and 200 kN). The prestressing pullout load was applied using the jacking system that includes a hydraulic pump and control unit mounted on a mobile frame. This jack is commonly employed for the tensioning of steel strands in prestressed concrete members. The information related to all eight specimens including the level of pre-stress, and concrete strength is presented in Table 1.

Table 1: Manufactured specimens for Phase II study

Manufacturer assigned ID	Report assigned ID	Pre-stressing force (kN)	Concrete strength* (MPa)	Concrete stress due to pre-compression* (MPa)	Bar tensile stress (MPa)
7	A1	236.6	72	1.49	349
8	A2				
13	B1	277.3		1.75	409
14	B2				
15	C1	195.9		1.23	289
16	C2				
17	D1	236.6	43.2	1.49	349
18	D2				

*Characteristic compressive strength of concrete cubes

Table 2 summarizes the configurations of the specimens and their respective loading protocols. As it is evident from Table 1, all specimens have a uniform configuration with a length of 4000 mm, and a uniform section property as illustrated in Figure 9.

Table 2: Configuration of PC SEAHIVE® samples

Specimen ID	Length (mm)	Hole diameter external/internal (mm)	Height (mm)	Width (mm)	Thickness (mm)
A1/2	4000	228/194	791.9	914.9	127
B1/2					
C1/2					
D1/2					

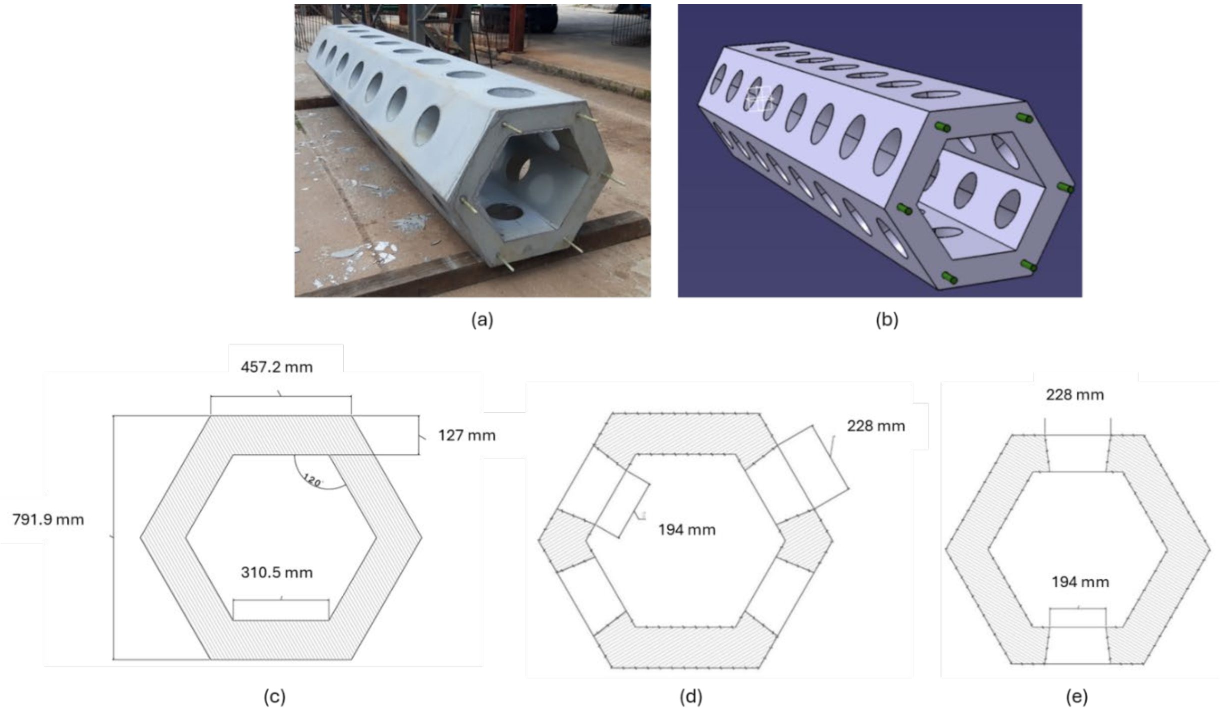

Figure 9: Geometry of PC SEAHIVE® unit: (a) PC SEAHIVE® at the test site; (b) PC SEAHIVE® modeled in Abaqus software; (c) solid cross-sectional view with dimensions; (d) cross-sectional view with four holes; (e) cross-sectional view with two holes

Materials

GFRP Characterization

In this study, six M13 (#4) GFRP bars were pre-stressed as reinforcement for the PC SEAHIVE® elements. The mechanical properties of M13 GFRP bars were reported by the manufacturer. Some properties did not align with the values suggested by ASTM D7957 [30]. A comparison between the reported properties and the corresponding specification values is presented in Table 3. The reported data indicates a nominal diameter of 12 mm and a nominal cross-sectional area of 113 mm^2 which are both lower than the specification values of 12.7 mm and 129 mm², respectively. Despite the reduced dimension, the bars exhibited a higher failure load of 110 kN compared to the minimum spec value of 96 kN, corresponding to a tensile strength of 915 MPa, which exceeds the ASTM D7957 [30] minimum of 744 MPa. The measured tensile modulus was 50 GPa, also surpassing the minimum spec modulus of 46 GPa. The manufacturer's reported bond strength of the bars is 7.37 MPa.

Table 3: GFRP reinforcement characteristics

	Measured properties	**ASTM D7957**
Nominal Diameter (mm)	12	12.7
Nominal Area (mm^2)	113	129
Failure force (kN)	110	96
Tensile strength (MPa)	915	744
Modulus (GPa)	50	46

Concrete Characterization

The compressive strength of concrete was evaluated using the standard cube test method, carried out in accordance with EN 12390-3 [28]. In this procedure, concrete specimens are cast in cube molds and cured under controlled conditions until the designated testing age is reached. The cubes are then placed in a compression testing machine, where a monotonically increasing axial load is applied until failure occurs. The maximum load at failure is divided by the cross-sectional area of the cube to obtain compressive strength. The summary of cube test results is included in Table 4.

Table 4: Cube test results

Specimen ID	**A1**	**A2**	**B1**	**B2**	**C1**	**C2**	**D1**	**D2**
Max Compressive Strength (MPa)	80.53	82.25	75.64	80.44	71.45	77.39	56.49	N/A
Mean Compressive Strength (MPa)	79.80	81.00	71.63	79.56	70.96	74.46	55.38	N/A
Guaranteed Compressive Strength (MPa)	77.70	79.40	68.20	78.43	70.20	72.44	52.05	N/A
Max Density ($^{kg}/_{m^3}$)	2489.2	2463.7	2455.1	2460.1	2448.9	2457.2	2428.4	N/A
Mean Density ($^{kg}/_{m^3}$)	2476.3	2446.7	2442.8	2449.9	2430.7	2453.3	2425.6	N/A
Guaranteed Density ($^{kg}/_{m^3}$)	2444.7	2428.1	2433.5	2444.1	2417.2	2448.3	2409.9	N/A

To derive cylinder-equivalent compressive strengths from the 150×150 mm cube results, the commonly used correlation for normal-weight concrete tested at the same age $\left(f'_{c,cyl} = 0.80\ f'_{c,cube}\right)$ was adopted [31]. The equivalent cylinder test results are reported in Table 5.

Table 5: Equivalent cylinder compressive strength

Specimen ID	A1	A2	B1	B2	C1	C2	D1	D2
Max (MPa)	64.4	65.8	60.5	64.4	57.2	61.9	45.2	N/A
Mean (MPa)	63.8	64.8	57.3	63.6	56.8	59.6	44.3	N/A
Guaranteed (MPa)	62.2	63.5	54.6	62.7	56.2	58.0	41.6	N/A

Test Set-up and Instrumentation

The four-point bending tests were performed in a reaction frame using a vertical servo-hydraulic actuator that applied load through a steel spreader beam with two loading rollers that produce two equal line loads on the specimen’s top face. As schematically presented in Figure 10, the PC SEAHIVE® unit was simply supported on steel rollers. The resultant free span was 3,928 mm with a 36 mm overhang beyond the left and right support. The distance from the nearest support to the nearest loading line, known as shear arm, was 1,224 mm, and the spacing between the two loading lines defined a constant-moment region of 1,480 mm. This setup generated the classic four-point bending condition.

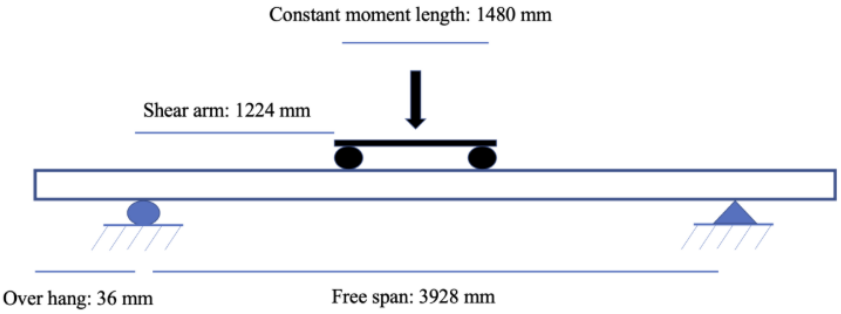

Figure 10: schematic representation of test setup

Loading Protocol

Quasi-static load protocols were used in all four-point flexural tests. The two supports were positioned 0.2125 m from each end, while the two loading plates were located 1.48 m from the ends. This symmetric configuration facilitates rotational freedom about the longitudinal axis, thereby enabling the specimen to fully arrive to its flexural strength. For all tests, a quasi-static cyclic load protocol was adopted. In this procedure, load was applied in progressively increasing cycles to permit detailed inspection of cracking patterns and specimen behavior at incremental load levels, followed by a final cycle taken to failure.

RESULTS AND DISCUSSION

This section presents the crack patterns and load–displacement response of seven PC SEAHIVE® specimens. Due to the presence of holes in various sections of the specimens it is of interest to measure the characteristics of each section as presented in Table 6, and demonstrated in Figure 11 where S_t refers to section modulus which is equal to $\frac{I}{c}$ where I stands for moment of inertia, and c is the distance from the neutral axis to the extreme fiber in tension. Cross-sectional area is specified by A. It should be noted that while cross-sections 1, 2 and 3 represent real situations, cross-section 4 is only ideal and represents the case of the six perforations all at the same location. It was included as a lower-bound case in terms of geometrical properties.

Each specimen is analyzed to determine its analytical cracking load. For this purpose, Eq (1) is utilized to measure the concrete modulus of elasticity based on ACI 318-19 [20]. Where f_c' is the cylinder compressive strength of concrete.

$$E_c = 4700\sqrt{f_c'} \tag{1}$$

Effective flexural stiffness of the beam specimen subject to four-point bending is calculated using Eq (2) where L is the distance between supports that equals 3,928 mm, and a is the distance from each support to the nearest load point that equals 1,224 mm.

$$K = \frac{24EI}{a(3L^2 - 4a^2)} \tag{2}$$

The concrete modulus of rupture (f_r) is calculated using Eq (3) where λ represents modification factor for lightweight concrete. Since all samples of PC SEAHIVE® are constructed from normal-weight concrete, the modification factor equals 1.0.

$$f_r = 0.62\,\lambda\sqrt{f_c'} \tag{3}$$

Cracking moment (M_{cr}) in pre-stressed members can be calculated using Eq (4). The prestressing force differs for the specimen pairs identified as A1/2, B1/2 and C1/2 (D1/2=A1/2).

$$M_{cr} = S_t\left(f_r + \frac{P_{prestress}}{A}\right) \tag{4}$$

Based on the geometry of the four-point bending test setup, cracking load (P_{cr}) can be calculated using Eq (5).

$$P_{cr} = \frac{2M_{cr}}{1.224} \tag{5}$$

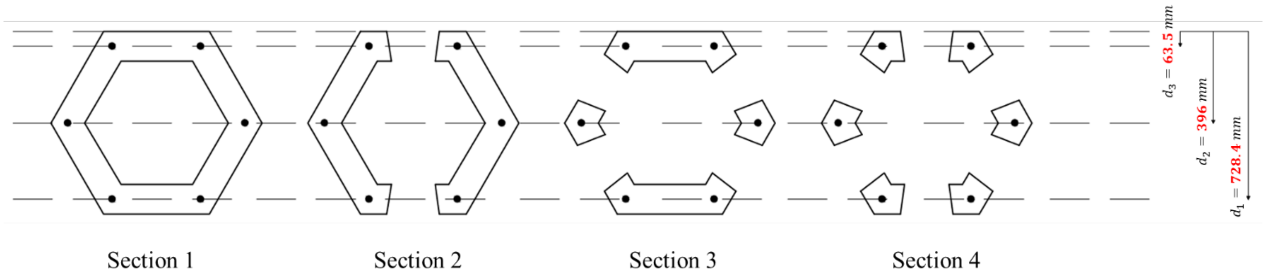

Figure 11: Proposed PC SEAHIVE® sections for analysis

Table 6: summary of PC SEAHIVE® section characteristics

Section #	Description	$A(mm^2)$	$I(mm^4)$	$c(mm)$	$S_t(mm^3)$
1	No holes at cross-section	291416	18601959834	396	46974646
2	Flange holes at cross-section	233348.2	12225295767	396	30871959
3	Web holes at cross-section	181753.5	15287595793.3	396	38605039.9
4	Flange and web holes at cross-section	123685.1	8910931726.2	396	22502352.8

Specimen A1

Under four-point bending, the first audible and visible distress was flexural cracking manifested by two vertical fissures nucleating from the tensile fiber region within the mid-leg at the “bottom flange” perforations and propagating into the solid parts of the side-legs (“web”) as seen in Figure 12. These cracks occurred before any discernible shear cracking, and additional fine flexural cracks likely developed along the bottom face outside the camera’s view.

With continued loading, the transference of load from flexural to shear mechanisms precipitated the formation of a horizontal crack across the mid-legs (top and bottom) and side-legs at one end of the specimen, as found in Figure 13, which coincided with a transient plateau in the load–displacement response (see Figure 14). This instance may indicate a transition from flexure to a flexure–shear/arching mechanism, observed in Figure 13. At one of the two ends of the specimen, the effective prestress may have been lower due to transfer-length effects, that promoted diagonal tension and localized damage and explained the asymmetric crack propagation toward a single loading point. Consistent with pretensioned behavior, prestress was more fully developed at midspan and at the opposite end.

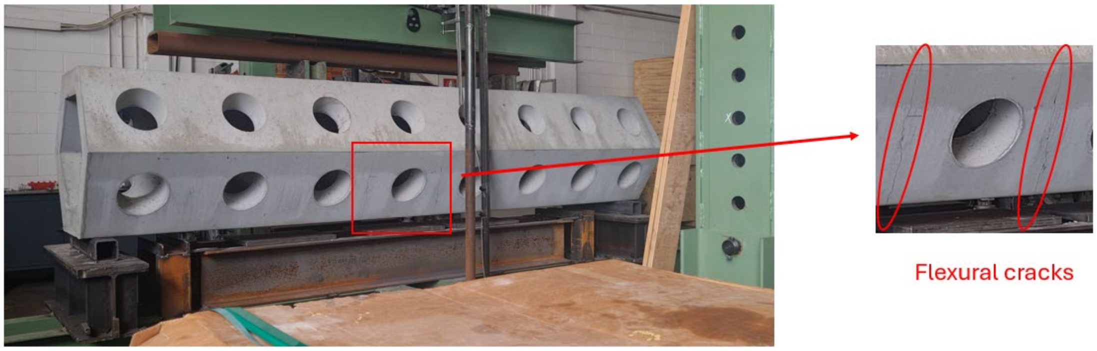

Figure 12: Flexural crack formation at specimen A1

Figure 13: Damaged representation of specimen A1

This trend is expected in pretensioned members because the prestressing force is transferred gradually from the bar to the concrete over the transfer length, so full precompression is not achieved until a distance away from the ends [32]. Coupled with end-zone stresses, this produces a region that is more vulnerable to wider cracking under shear-dominated demand. End-region cracking and reduced precompression near supports have been extensively documented for prestressed members and are mitigated by proper end-zone detailing and adequate development length [33]. Where the prestress is fully effective (midspan), the induced longitudinal prestressing suppresses flexural tension, raises cracking load, and reduces crack widths. However, near the supports the combination of limited effective prestress and high shear promotes earlier and wider inclined cracking. Collectively, the observed crack-width gradient evidence the greater effectiveness of prestressing in the middle span and underscores the need for robust end-zone reinforcement/anchorage to fully capitalize on prestress benefits under shear.

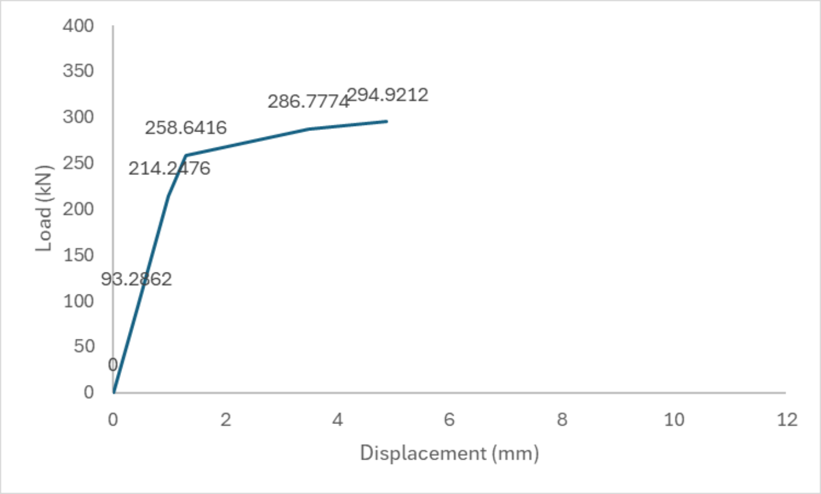

Figure 14: Load-displacement curve of specimen A1

Figure 14 shows the complete load–displacement response of specimen A1 under four-point bending. The structural behavior of specimen A1 fits two linear trends to quantify stiffness on either side of first cracking. The pre-cracking (flexural) branch has a slope of 216.0 kN/mm that represents effective flexural stiffness. After flexural cracks form, the tangent stiffness reduces dramatically, and the curve flattens before degrading toward failure. According to Figure 14, the cracking load is at about 214 kN.

The comparison between effective flexural stiffness of the specimen with the test result is presented in Figure 15. The idealized cross-sections, as extended in Table 6, are used to predict the measured flexural stiffness from the test. The calculations show that the exclusion of holes from the cross-section leads to unrealistic analytical prediction of the flexural stiffness of specimen A1.

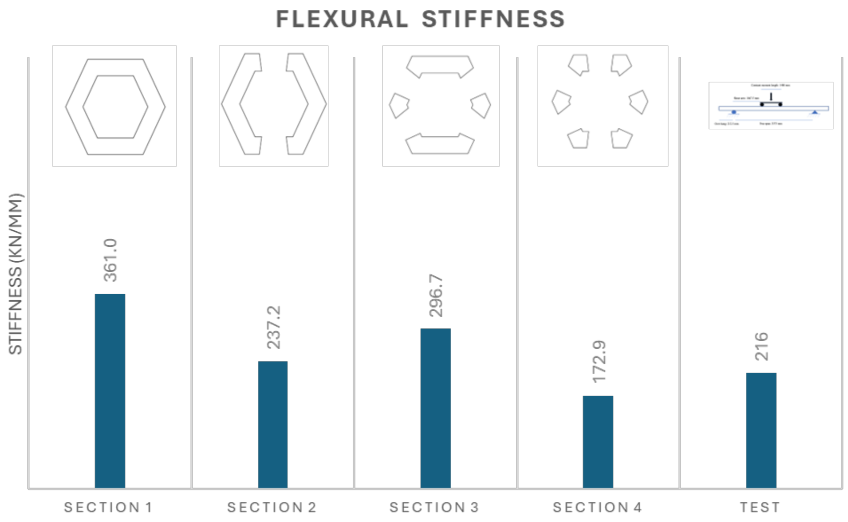

Figure 15: Effective flexural stiffness of specimen A1 in different sections vs. experimental stiffness

Rupture modulus of specimen A1 is 5.26 MPa. Figure 16 provides an analytical calculation of crack load (P_{cr}) based on Eq (4) compared to the test result. The section that included all the holes had the most realistic result in comparison to the test outcome. A summary of analytical and experimental structural characteristics of specimen A1 is presented in Table 7.

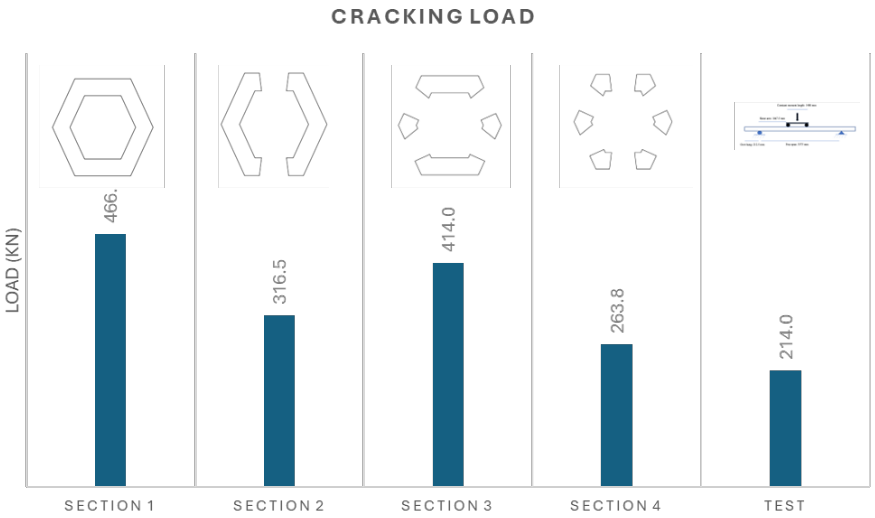

Figure 16: Cracking load of specimen A1 in different sections vs. experimental crack load

Table 7: Specimen A1 analysis summary

Characteristics	Analytical	Experimental
$K\ \left({}^{kN}/_{mm}\right)$	172.9	216.0
$M_{cr}\ (kN.m)$	161.4	131.0
$P_{cr}(kN)$	263.8	214.0

Specimen A2

Under four-point bending, Specimen A2 first showed flexural cracks initiating at the bottom flange perforations and propagating upward into the web (Figure 17). These cracks formed before any shear distress was observed. With increasing load, a horizontal crack developed near one end of the unit (Figure 18), signaling a shift from flexural to combined flexure–shear behavior. This coincided with the plateau in the load–displacement curve (Figure 19). Damage concentrated near the weaker end, while midspan remained better confined by fully developed prestress. As already discussed, this behavior is typical of pretensioned members, where partial prestress near the supports makes these regions more vulnerable to diagonal cracks. Proper end-zone reinforcement is needed to mitigate such effects.

Figure 17: Flexural crack formation at specimen A2

Figure 18: Damaged representation of specimen A2

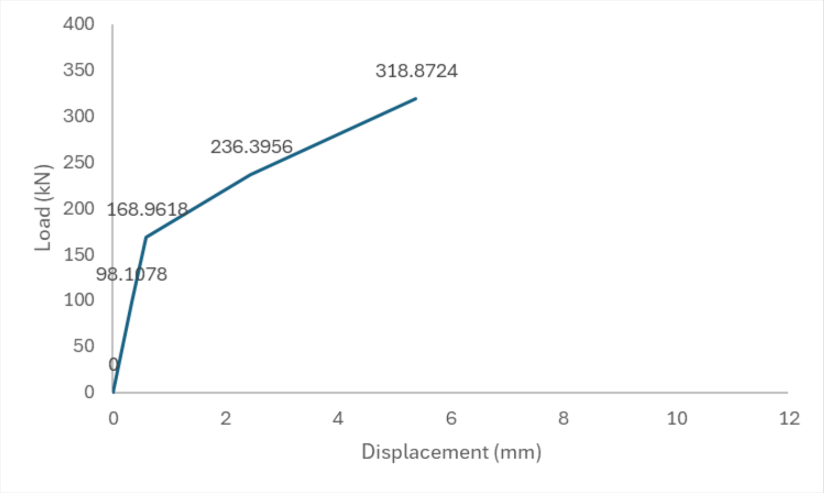

Figure 19: Load-displacement curve of specimen A2

The comparison between the effective flexural stiffness of the specimen and the measured test results is shown in Figure 20. Figure 21 represents the same comparison for the cracking load of specimen A2. Idealized cross-sections, as presented in Table 6, were used for the calculations. The results show that neglecting the perforations in the section leads to unrealistic analytical predictions of the flexural stiffness for Specimen A2. The summary of analytical vs. experimental results is tabulated in Table 8.

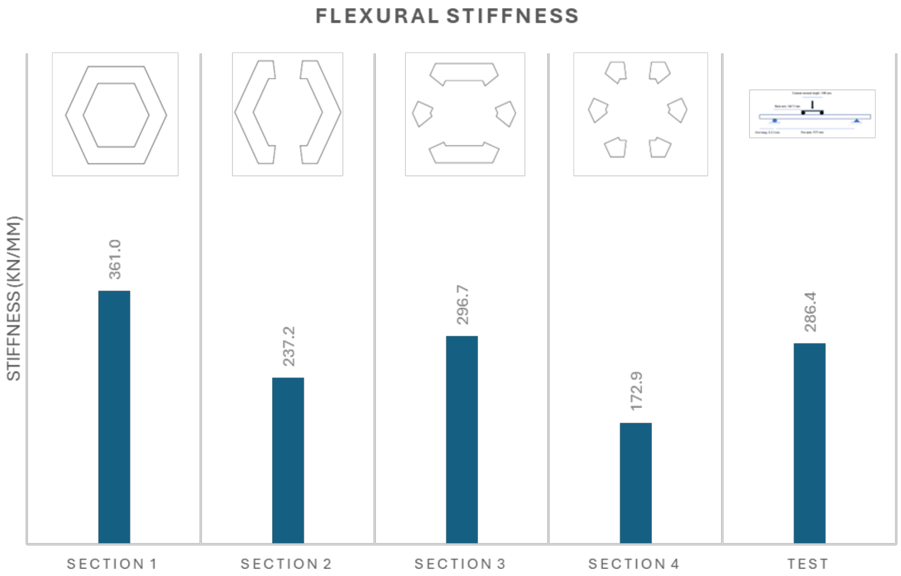

Figure 20: Effective flexural stiffness of specimen A2 in different sections vs. experimental stiffness

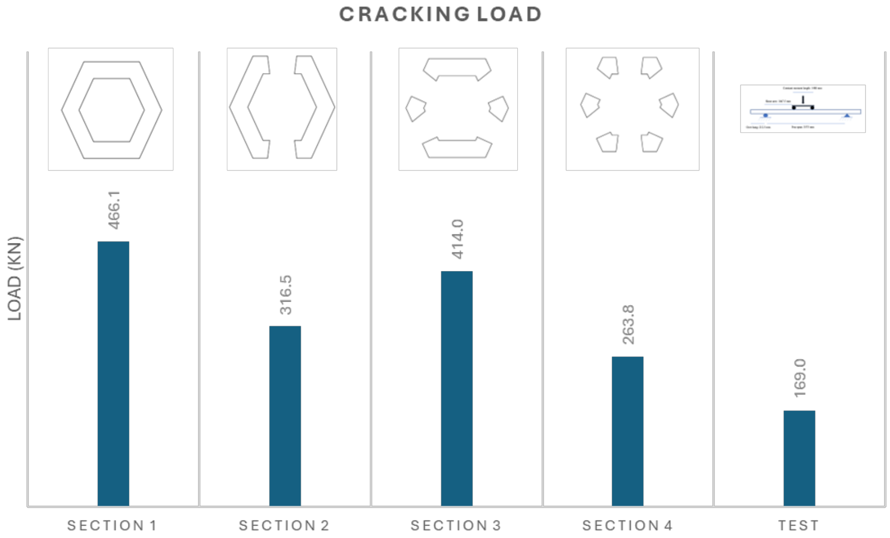

Figure 21: Cracking load of specimen A2 in different sections vs. experimental crack load

Table 8: Specimen A2 analysis summary

Characteristics	Analytical	Experimental
$K\left({}^{kN}/_{mm}\right)$	172.9	286.4
$M_{cr}\ (kN.m)$	161.4	103.4
$P_{cr}(kN)$	263.8	169

Specimen B1

First distress was flexural cracking along the bottom flange between perforations (Figure 22). With continued loading a horizontal mid-leg crack formed and branched into diagonal (flexure–shear) cracks toward one end (Figure 23), followed by progressive end-region damage seen in the cross-section view. The load–displacement curve (Figure 24) shows a marked knee at about 274 kN and a shallow post-cracking slope to a peak near 345 kN. Prestress adds longitudinal precompression, so the net tensile stress at the extreme fiber is smaller at a given load. Consequently, the measured cracking load 273.6 kN nearly matches the analytical prediction 275.9 kN and is higher than A2 (169 kN) and comparable to A1 (271 kN) despite identical concrete strength. This is the clearest benefit of the higher prestress. Gross flexural stiffness is governed mainly by the value of EI of the perforated shell. The measured pre-cracking stiffness 101 kN/mm is well below the analytical 172.9 kN/mm and below A1, and A2, which might have been caused by local seating/slip at supports and load points.

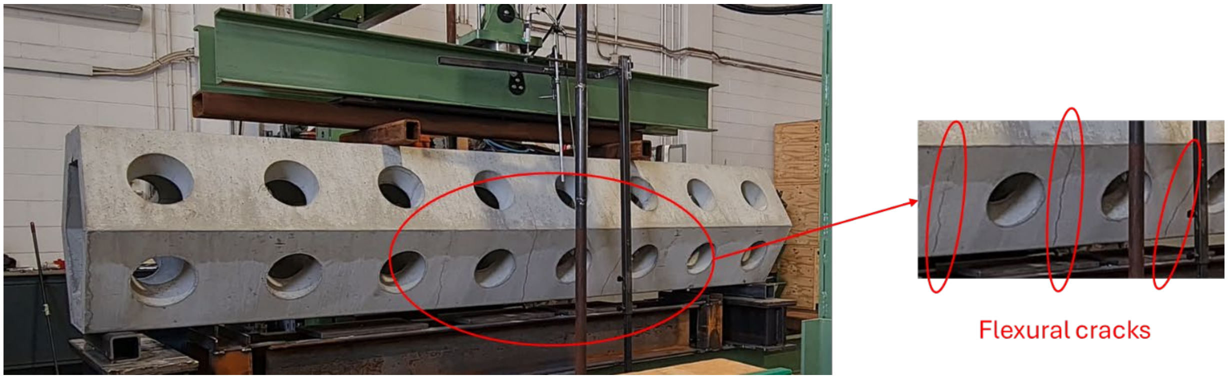

Figure 22: Flexural crack formation at specimen B1

Figure 23: Damaged representation of specimen B1

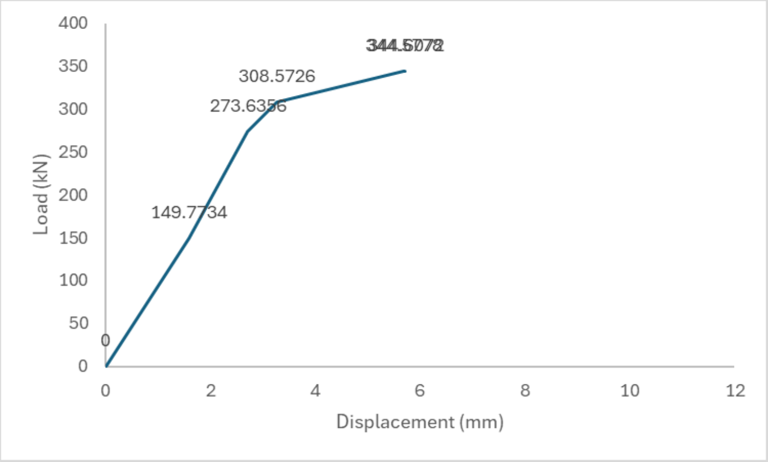

Figure 24: Load-displacement curve of specimen B1

As presented in Figure 25, although idealized sections overpredict flexural stiffness, ignoring perforations and shear deformation yields unrealistic stiffness for the test article. According to Figure 26, and the summary at Table 9, analytical cracking load aligns well with the test.

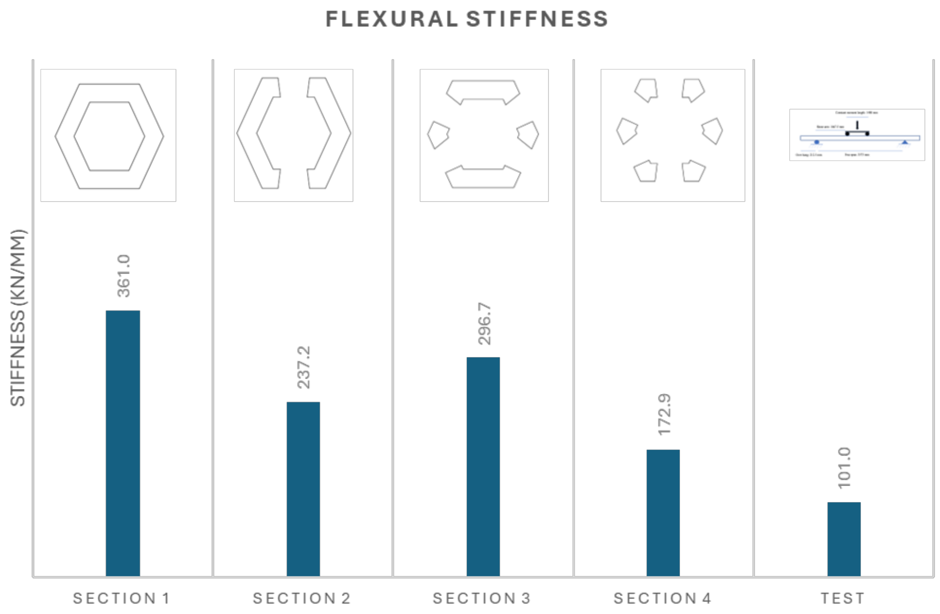

Figure 25: Effective flexural stiffness of specimen B1 in different sections vs. experimental stiffness

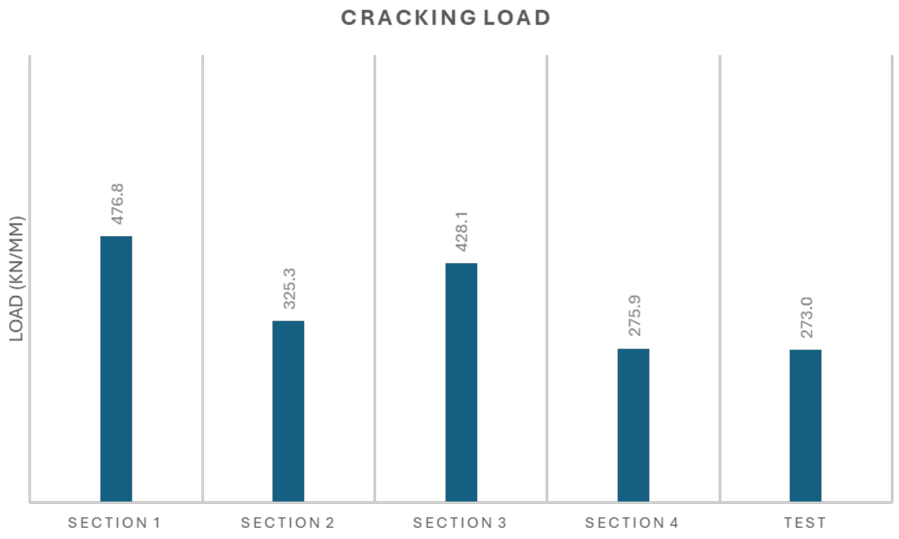

Figure 26: Cracking load of specimen B1 in different sections vs. experimental crack load

Table 9: Specimen B1 analysis summary

Characteristics	Analytical	Experimental
$K\left({}^{kN}/_{mm}\right)$	172.9	101.3
$M_{cr}\ (kN.m)$	168.8	167.4
$P_{cr}(kN)$	275.9	273.6

Specimen B2

Flexural cracks initiated at the bottom-flange perforations and grew into the web (Figure 27). With further loading, cracking localized and broadened near one end (Figure 28). The load–displacement curve (Figure 29) is bilinear with a knee at 237.7 kN and a peak near 318 kN. The tested pre-cracking stiffness is 330.1 kN/mm. Pre-cracking stiffness reflects the specimen and testing system. B2 likely had better seating compared to B1.

Figure 27: Flexural crack formation at specimen B2

Figure 28: Damaged representation of specimen B2

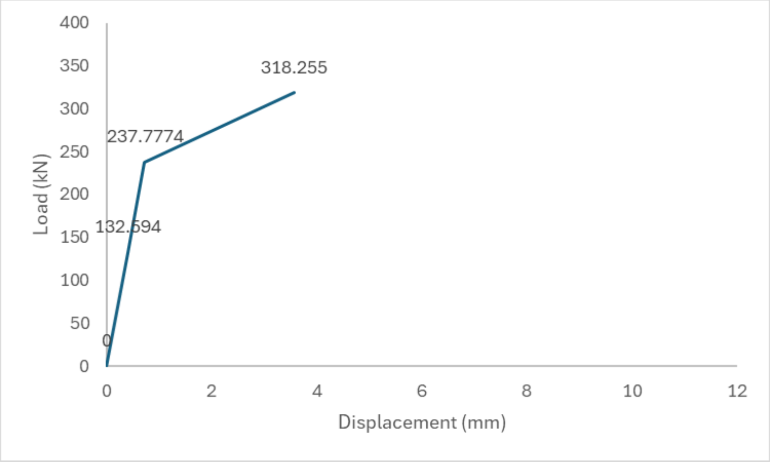

Figure 29: Load-displacement curve of specimen B2

According to Figure 30 and Figure 31, simplified analytical sections overpredict stiffness and cracking load when perforations and system compliance are not fully captured. A comparison of analytical vs. experimental results are presented in Table 10.

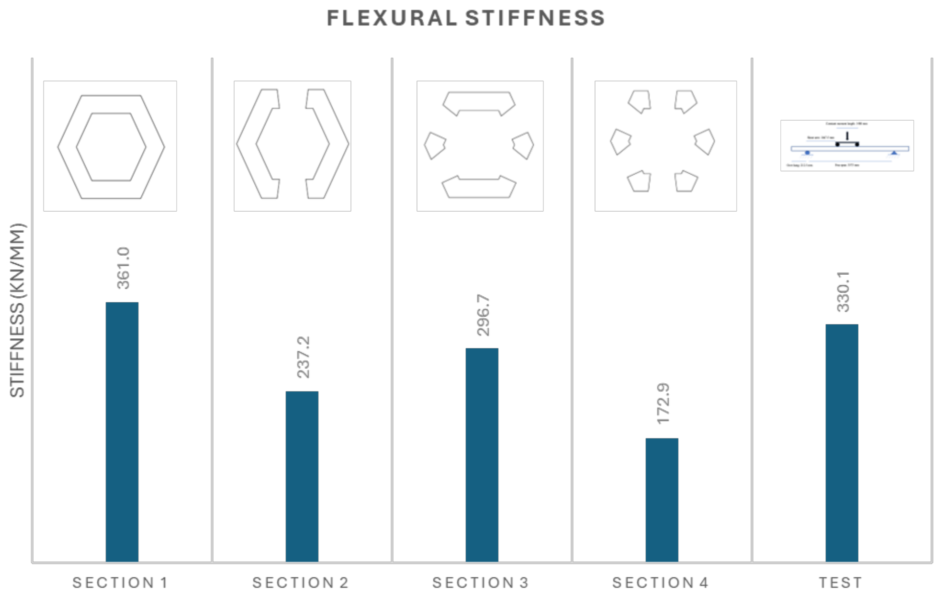

Figure 30: Effective flexural stiffness of specimen B2 in different sections vs. experimental stiffness

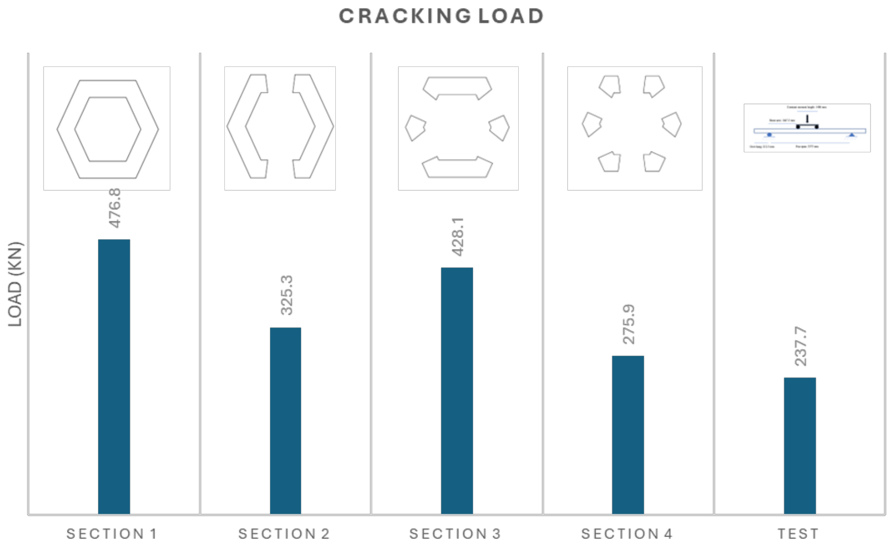

Figure 31: Cracking load of specimen B2 in different sections vs. experimental crack load

Table 10: Specimen B2 analysis summary

Characteristics	Analytical	Experimental
$K\left({}^{kN}/_{mm}\right)$	172.9	330.1
$M_{cr}\ (kN.m)$	168.8	167.5
$P_{cr}(kN)$	275.9	237.7

Specimen C1

Flexural cracks initiated at the bottom-flange perforations within the constant-moment region (Figure 32) and propagated into the web. With further loading a horizontal mid-leg crack formed toward one end and merged with diagonal cracks (Figure 33). The load–displacement curve (Figure 34) shows a knee at 187.7 *kN* and a very low pre-cracking slope, giving 69.3 *kN/mm*. With less longitudinal precompression, the net tensile stress at the extreme fiber rises faster under bending. That lowers the cracking load 187.7 kN vs the 270–275 kN observed in the higher-prestressed specimens. The crack pattern concentrates at perforation rims where stress concentrations are highest.

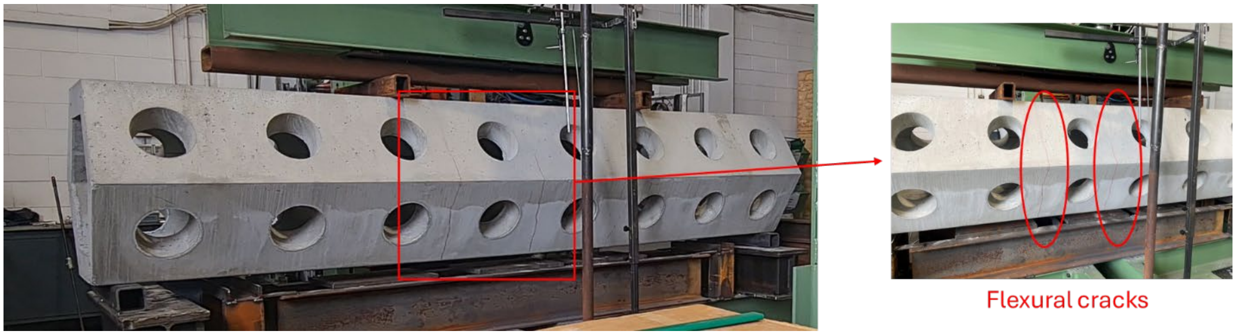

Figure 32: Flexural crack formation at specimen C1

Figure 33: Damaged representation of specimen C1

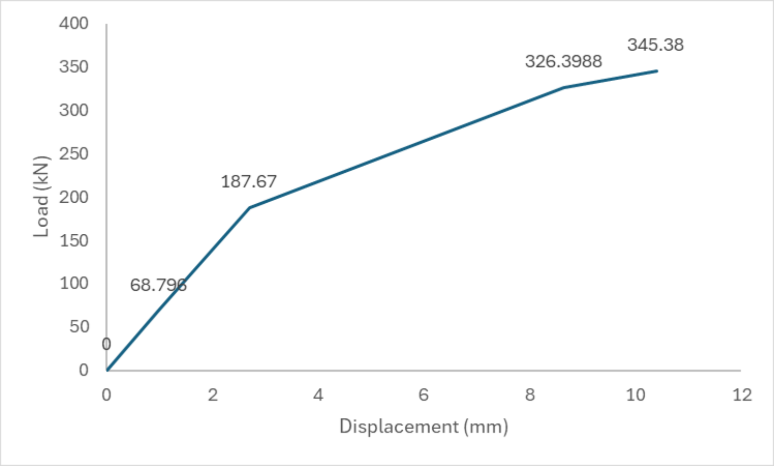

Figure 34: Load-displacement curve of specimen C1

According to Figure 35, and Figure 36, idealized sections overpredict stiffness and cracking load because they do not fully capture perforation-induced stress concentrations, early microcracking, and test-system compliance. Table 11 summarizes analytical vs. experimental characteristics of specimen C1.

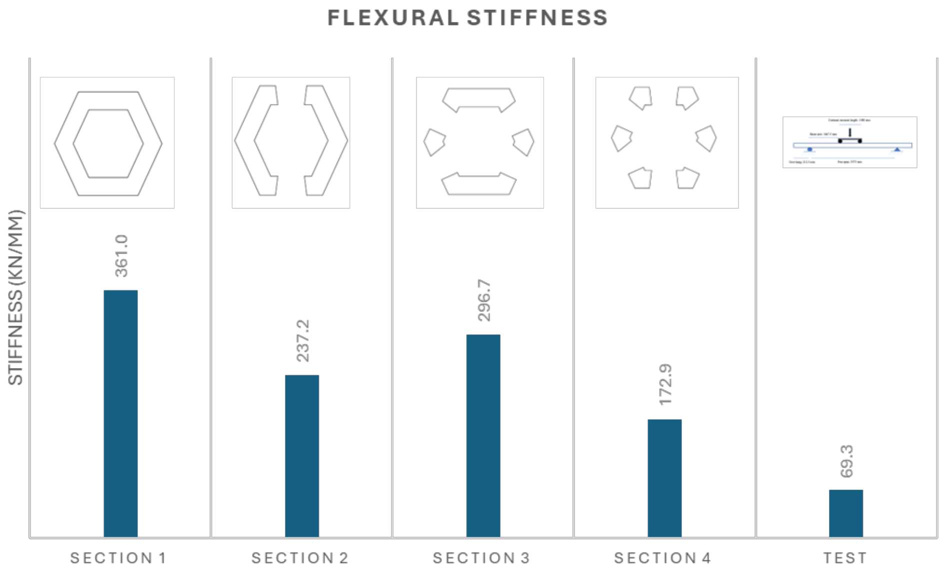

Figure 35: Effective flexural stiffness of specimen C1 in different sections vs. experimental stiffness

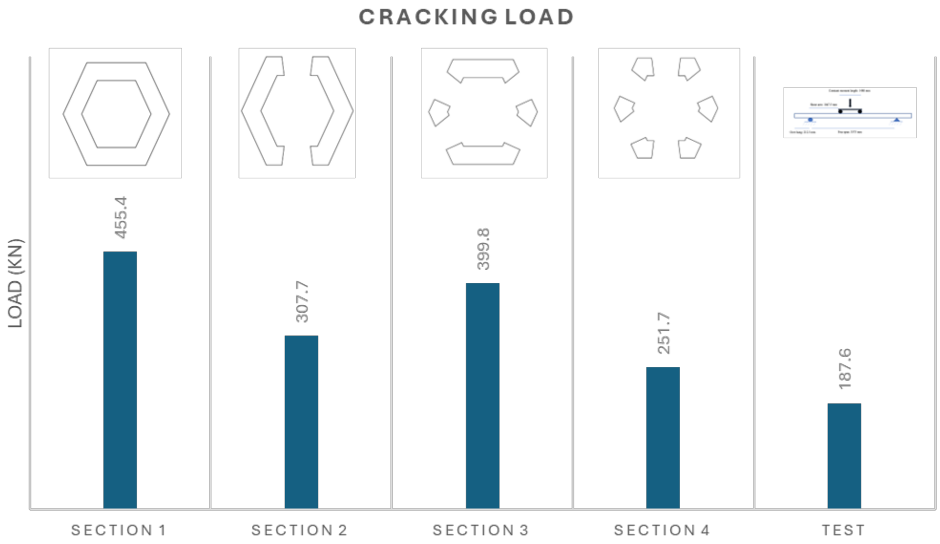

Figure 36: Cracking load of specimen C1 in different sections vs. experimental crack load

Table 11: Specimen C1 analysis summary

Characteristics	Analytical	Experimental
$K\left({}^{kN}/_{mm}\right)$	172.9	69.3
$M_{cr}\ (kN.m)$	154.0	114.9
$P_{cr}(kN)$	251.7	187.7

Specimen C2

First distress was flexural cracking at the bottom-flange perforations in the constant-moment zone (Figure 37). With increasing load, a horizontal mid-leg crack formed toward one end and linked with inclined cracks (Figure 38), marking a shift from flexure to flexure–shear. The load–displacement curve (Figure 39) shows a knee at 180.4 kN and a very shallow pre-cracking slope, giving 62.3 kN/mm. the post-cracking branch is soft up to a peak near 295 kN.

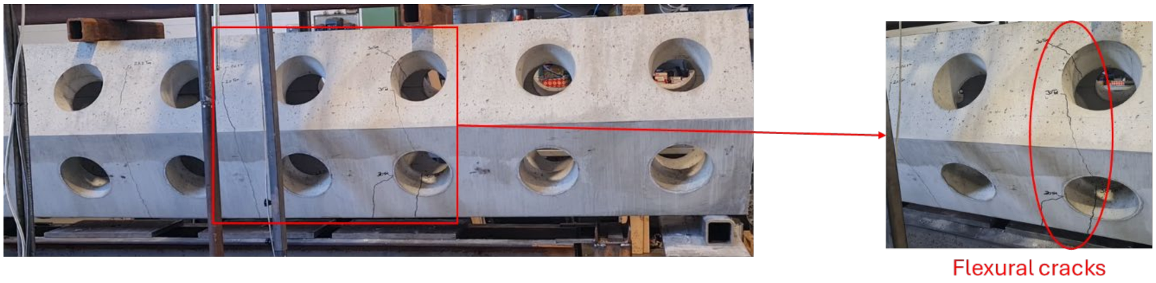

Figure 37: Flexural crack formation at specimen C2

Figure 38: Damaged representation of specimen C2

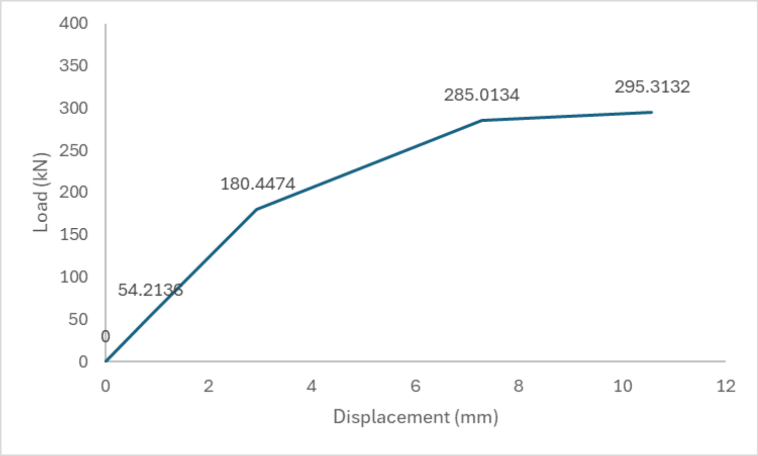

Figure 39: Load-displacement curve of specimen C2

According to Figure 40, and Figure 41, the same behavior as specimen C1 is observed at specimen C2. Table 12 presents a summary of test vs. analytical results for specimen C2.

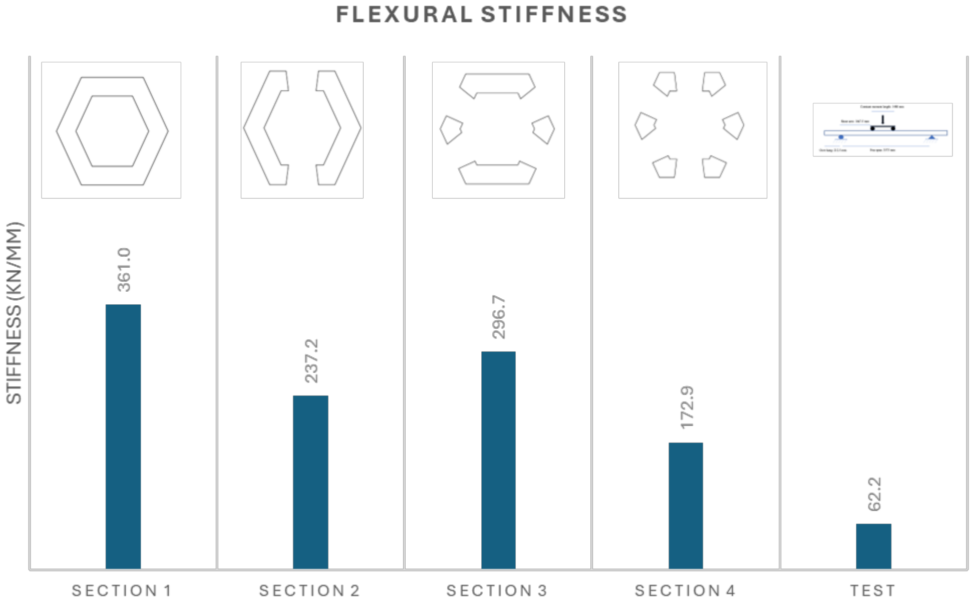

Figure 40: Effective flexural stiffness of specimen C2 in different sections vs. experimental stiffness

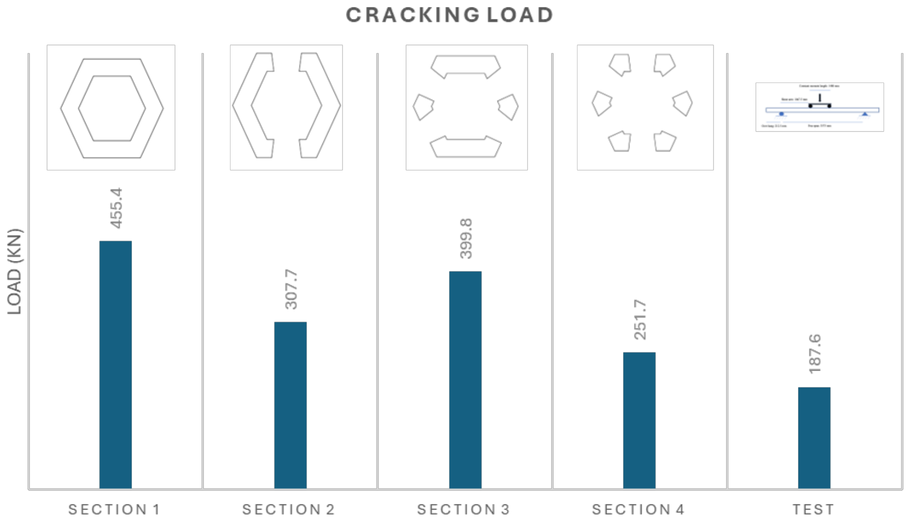

Figure 41: Cracking load of specimen C2 in different sections vs. experimental crack load

Table 12: Specimen C2 analysis summary

Characteristics	Analytical	Experimental
$K\ \left({}^{kN}/_{mm}\right)$	172.9	62.3
$M_{cr}\ (kN.m)$	154.0	110.4
$P_{cr}(kN)$	251.7	180.4

Specimen D1

The behavior of specimen D1 under four-point bending was similar to specimen A1. Initially, two vertical flexural cracks formed at the bottom flange perforations within the mid-leg region that propagated upward into the web, as shown in Figure 42. These cracks occurred before any visible shear cracks, with additional fine flexural cracks likely developing along the bottom face outside the camera's view. As the load increased, the mechanism transitioned from flexure to shear, marked by the formation of a horizontal crack across the mid-leg at one end of the specimen (Figure 43) and a transient plateau in the load–displacement curve (Figure 44). In line with typical pretensioned member behavior, prestress was fully developed near midspan which resulted in enhancing cracking resistance and reducing crack widths there. However, near the supports, where prestress was limited and shear demand was high, earlier and wider inclined cracks formed. The observation of crack-width gradient emphasizes the importance of proper end-zone detailing and anchorage design to fully utilize the benefits of prestressing under shear-dominated conditions.

Figure 42: Flexural crack formation at specimen D1

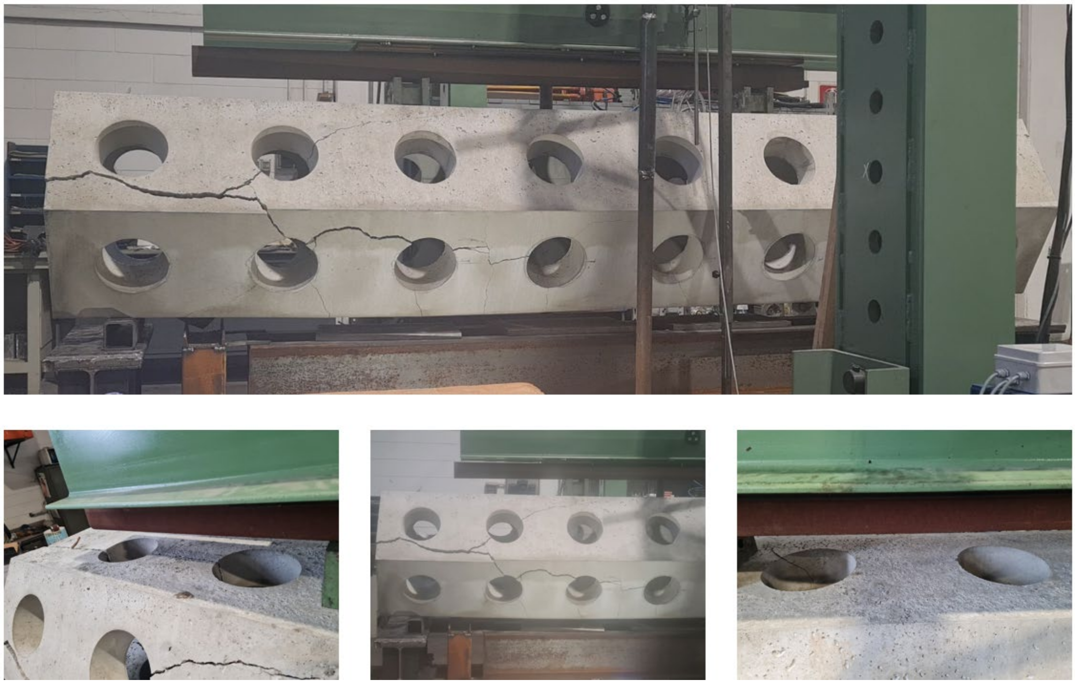

Figure 43: Damaged representation of specimen D1

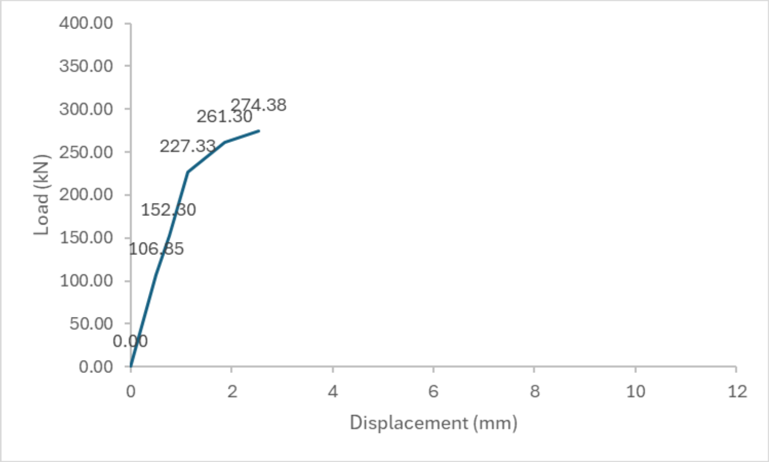

Figure 44: Load-displacement curve of specimen D1

Figure 44 presents the full load–displacement response of specimen D1 under four-point bending. The initial pre-cracking branch has a slope of 200.3 kN/mm, representing the effective flexural stiffness, while after cracking, the tangent stiffness drops significantly. The transition between these slopes identifies the cracking load, which occurs at approximately 227.3 kN.

The comparison between the effective flexural stiffness of specimen D1 and the test results is shown in Figure 45. The idealized cross-sections provided in Table 6 were used to predict the specimen's flexural stiffness. The analysis demonstrates that neglecting the presence of holes in the cross-section leads to overly high and unrealistic analytical predictions that highlight the importance of accurately modeling the perforations to properly capture the structural behavior of specimen D1.

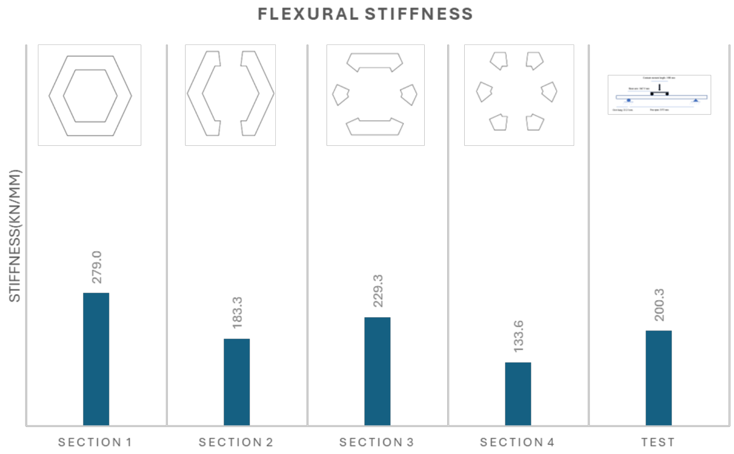

Figure 45: Effective flexural stiffness of specimen D1 in different sections vs. experimental stiffness

The rupture modulus of specimen D1 is 4.08 MPa. Figure 46 illustrates the analytical calculation of the cracking load P_{cr} using Eq (4), compared with the experimental test results. Among the different section models analyzed, the section that fully accounted for all the holes provided the most realistic prediction, closely matching the observed test behavior. A comprehensive summary of both analytical predictions and experimental structural characteristics for specimen D1 is presented in Table 13.

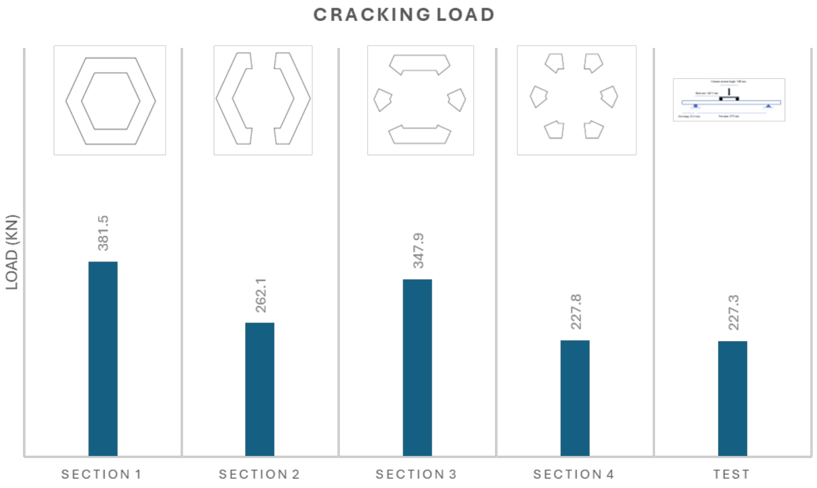

Figure 46: Cracking load of specimen D1 in different sections vs. experimental crack load

Table 13: Specimen D1 analysis summary

Characteristics	Analytical	Experimental
$K\left({}^{kN}/_{mm}\right)$	133.6	200.3
$M_{cr}\ (kN.m)$	139.4	139.1
$P_{cr}(kN)$	227.8	227.3

Specimen D2

This specimen was not tested. In future work, it will be externally wrapped with GFRP laminates to investigate shear capacity improvement.

FEM MODELING

To further investigate the observed cracking mechanisms, a finite-element method (FEM) model was developed in the Abaqus software package using the Concrete Damaged Plasticity (CDP) formulation. In the CDP formulation, stiffness degradation is captured via separate tensile and compressive damage variables and employs fracture-energy regularization in tension to achieve mesh-objective softening. Material inputs were calibrated to Sample D1's measured properties (compressive strength and density), and the perforated SEAHIVE® geometry was explicitly modeled as presented in Figure 47.

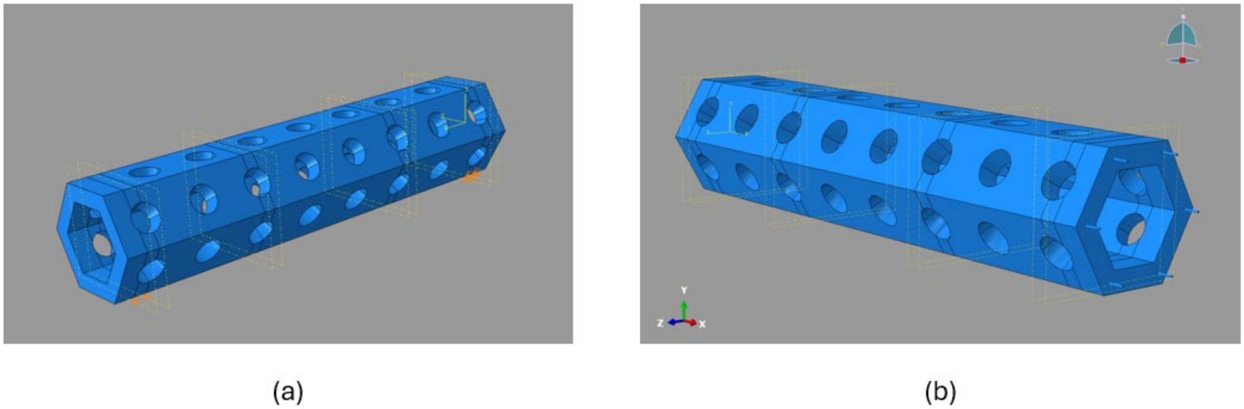

Figure 47: Specimen D1 PC SEAHIVE® FEM model in the Abaqus software (Geometry, and boundary conditions); (a) plain concrete, (b) concrete with GFRP reinforcement

According to Figure 48, the analysis of the plain concrete structure predicted a band of high tensile damage ($D_t \approx 0.8$) cutting across the web posts near mid-depth and stemming from the hole edges, while no compressive damage (crushing) accumulated along the principal compression struts. This pattern mirrors the test evidence of flexure–shear cracking that initiated by stress concentrations at perforation crowns and propagated towards load and support regions, with damage localizing where the effective shear area is reduced by the openings.

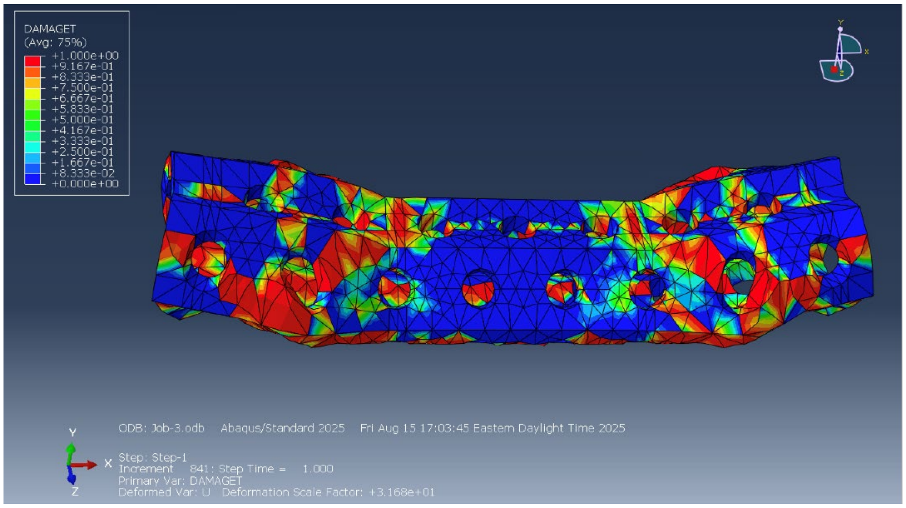

Figure 48: Damage results from Abaqus FEM model

In another FEM attempt for the plain concere case, a finer mesh was generated to discretize the structure using hexagonal linear interpolation 20-mm long elements as presented in Figure 49. This approach enhanced computational efficiency and eliminated mesh dependency, thereby preventing numerical instability within the model.

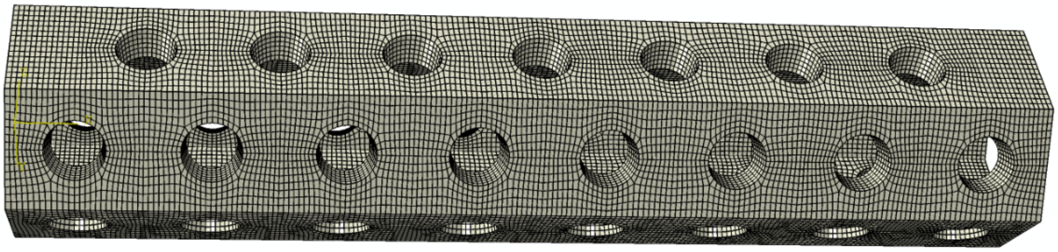

Figure 49: Fine-mesh representation of FEM model

A four-point bending configuration is utilized to replicate the desired test setup for the beam-like unit. In this arrangement, the applied loading is distributed across two distinct points located along the top surface of the structure, with a clear spacing of 1,432 mm between them. As presented in Figure 50, at the base of the structure, support conditions are carefully defined to replicate realistic boundary constraints: one end of the unit is supported by a roller that restricts vertical displacement in the y-direction only, while the opposite end is supported by a pinned connection that constrains motion in both the y- and z-directions. To further ensure physical accuracy and prevent the introduction of any non-representative or artificial movements, both support conditions are constrained from translating in the x-direction. This setup permits the structure to undergo deformation under loading, without imposing unrealistic boundary behavior that could compromise the validity of the results.

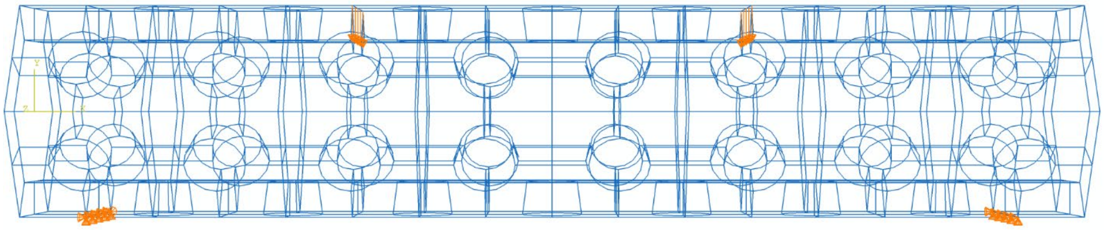

Figure 50: Representation of boundary conditions in FEM model

Figure 51 illustrates the tension damage distribution, effectively capturing both flexural and shear behavior within the model. The results align with previous findings and the observed stress patterns.

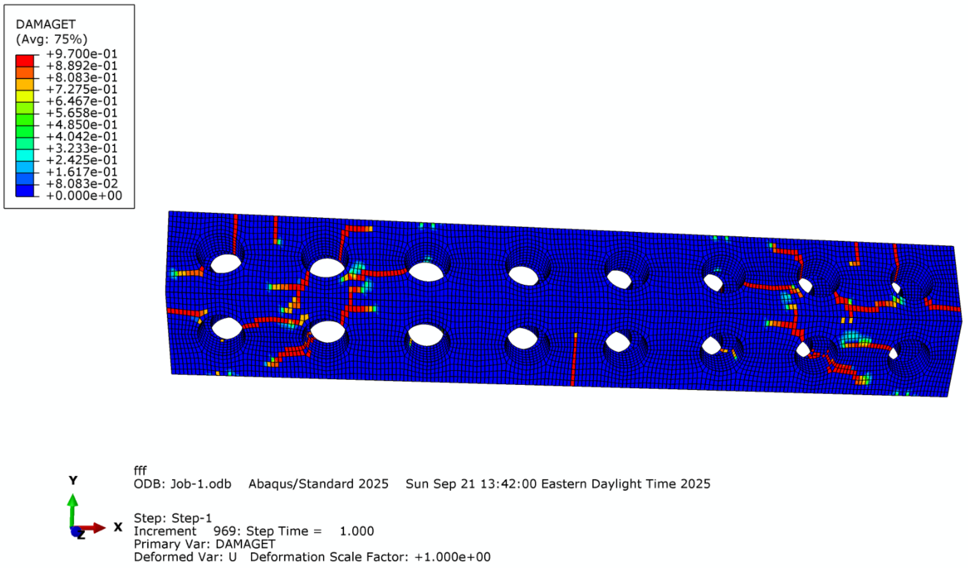

Figure 51: Tension damage distribution

The model as described assumed plain concrete with no embedded reinforcement, and no explicit prestress forces, which resulted in symmetric damage at both ends. In contrast, the experiment exhibited some asymmetric cracking, plausibly influenced by prestress transfer being more effective at one end, which would shift stress resultants and amplify tensile fields locally. For closer validation, the next FEM iteration should: (i) embed the GFRP bars and include pretension with a realistic transfer length; (ii) refine fracture energy, dilation angle, and end-zone confinement parameters to match crack onset and post-cracking stiffness; and, (iii) consider bond–slip or reduced tie stiffness where development is limited.

RECOMMENDATIONS AND CONCLUSIONS

This study focused on the structural performance evaluation of PC SEAHIVE® units reinforced internally with six prestressed GFRP bars. The experimental program included eight specimens (only seven of them tested and reported here) with different levels of pre-stressing, and concrete compressive strength. The overall performance of perforated hexagonal concrete elements under four-point bending tests was evaluated, and valuable insights into the flexural behavior, and cracking mechanisms of PC SEAHIVE® units were obtained. The results demonstrate the significant influence of prestressing force, perforation geometry, and level of reinforcement pretensioning on the load-displacement response and cracking resistance of the PC SEAHIVE® units.

As shown in Figure 52, two distinct stages are exhibited from the load-displacement curves of all specimens: an initial linear-elastic phase corresponding to the pre-cracking behavior, followed by a nonlinear phase marked by crack initiation and progressive damage. Specimens with higher prestressing forces, such as A1, A2, B1, and B2, demonstrated delayed onset of visible cracks compared to specimens with lower prestress levels, such as C1 and C2. This behavior highlights the role of prestressing in reducing tensile stresses, controlling crack widths, and enhancing the durability of PC SEAHIVE® units. Specimen D1, which utilized a lower concrete strength of 43 MPa has a lower pre-cracking stiffness compared to specimens A1, and A2 with the same prestressing level and higher concrete compressive strength. The cracking load for this specimen is close to the other two specimens and possibly the result of a different loading rate during the application of the loading protocol.

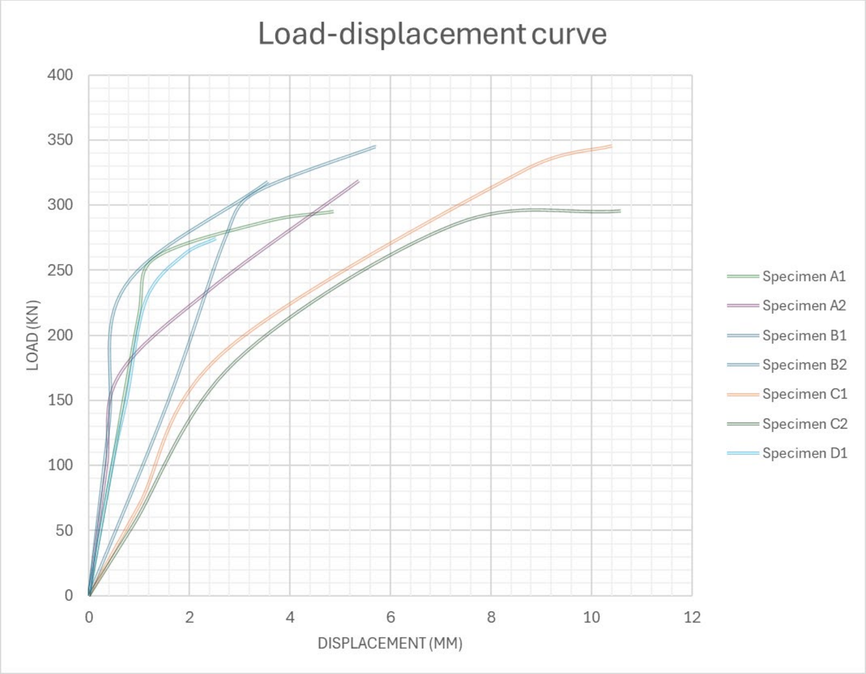

Figure 52: Load-displacement curve for all specimens

The analytical and experimental results summarized in Table 14 further emphasize the benefits of prestressing. For instance, the analytical cracking load predictions closely matched the experimental values for specimens A1, B1, B2, and D1, which validates the accuracy of the design methodology when perforations and prestress effects are adequately modeled. However, discrepancies were observed for specimens C1 and C2, where experimental cracking loads were lower than predicted. This suggests that the current analytical models may not fully account for the localized stress concentrations at perforation edges and the reduced shear area in highly perforated sections. Future models should incorporate these effects to improve prediction accuracy.

A clear correlation between prestressing force and cracking load can be observed from the comparison of the tested specimens. For instance, a superior cracking resistance was observed by specimens B1 and B2, which had the highest prestressing force of 277.3 kN, with cracking loads of 273.6 kN and 237.7 kN, respectively. In contrast, C1 and C2, with a prestressing force of 195.9 kN, exhibited lower cracking loads of 187.7 kN and 180.4 kN, respectively.

Table 14: Summary of analytical vs. experimental results for all specimens

Specimen ID	$f_c'\ (MPa)$	$P_{prestress}(kN)$	$K\ (kN/mm)$		$M_{cr}\ (kN.m)$		$P_{cr}(kN)$	
			Analytical	Experimental	Analytical	Experimental	Analytical	Experimental
A1	72	236.6	172.9	216.0	161.4	131.0	263.8	214.0
A2	72	236.6	172.9	286.4	161.4	103.4	263.8	169.0
B1	72	277.3	172.9	101.3	168.8	167.4	275.9	273.6
B2	72	277.3	172.9	330.1	168.8	145.5	275.9	237.7
C1	72	195.9	172.9	69.3	154.0	114.9	251.7	187.7
C2	72	195.9	172.9	62.3	154.0	110.4	251.7	180.4
D1	43	236.6	133.6	200.3	139.4	139.1	227.8	227.3
D2	N/A	N/A	N/A	N/A	N/A	N/A	N/A	N/A

From a serviceability perspective, specimens with higher prestress maintained narrower crack widths. The pre-cracking stiffness (*K*) was particularly high for A2 and B2, reaching 286.4 kN/mm and 330.1 kN/mm, respectively, as reported in Table 14. Conversely, C1 and C2 exhibited very low pre-cracking stiffness values of 69.3 kN/mm and 62.3 kN/mm, respectively. The low initial stiffness of these specimens (assuming it is not the result of testing inaccuracies) can lead to excessive deflections and reduced structural integrity under service loads.

A key observation from this study is the critical role of perforations in governing the structural response. While perforations enhance wave dissipation and provide ecological benefits, they also lead to stress rising, that lead to crack initiation around their rims. The observed crack patterns consistently originated at the perforation edges, confirming that these regions require special design attention.

Another important finding relates to the transition from flexural to flexure-shear behavior. As illustrated by the load-displacement curves in Figure 52, several specimens exhibited a plateau region that can possibly indicate a shift from pure flexural behavior to combined flexure-shear mechanisms. This transition was most prominent near the one end of specimens, where the effective prestress may have been lower due to transfer-length effects based on the procedure of bar detention. This highlights the need for proper end-zone detailing and sufficient development lengths for GFRP bars to ensure uniform prestress distribution and to minimize early diagonal, and horizontal cracking. To improve shear resistance, the ends of specimen D2 will be wrapped with pretensioned GFRP laminates and results will be provided in the report of Phase III.

Part of this study included FEM modeling that was able to capture the cracking mechanisms and validated the experimental observations. However, the current FEM model did not explicitly include the GFRP reinforcement or prestressing effects, which limited its ability to capture post-cracking behavior. Future work should focus on incorporating realistic reinforcement and prestress effects to improve the predictive capabilities of the simulation.

DATA AVAILABILITY STATEMENT

All data supporting the findings of this study are publicly available at https://doi.org/10.5281/zenodo.17427771.

REFERENCES

[1] N. Ocean, “Coastal Resource Management in Your State: States and Territories Working with NOAA on Ocean and Coastal Management,” *National Oceanic and Atmospheric Administration*, 2011.

[2] A. B. Smith, “US Billion-dollar weather and climate disasters, 1980-present,” 2022.

[3] J. R. Houston, “The economic value of beaches: a 2008 update,” *Shore and beach*, vol. 76, no. 3, pp. 22–26, 2008.

[4] M. Ghiasian *et al.*, “Laboratory quantification of the relative contribution of staghorn coral skeletons to the total wave-energy dissipation provided by an artificial coral reef,” *Journal of marine science and engineering*, vol. 9, no. 9, p. 1007, 2021.

[5] G. A. Maul and I. W. Duedall, “Demography of coastal populations,” in *Encyclopedia of coastal science*, Springer, 2019, pp. 692–700.

[6] M. Mirdarsoltany, “Solution for Implementation of Perforated Concrete Elements in Coastal Protection Systems: Experimental Testing and FEM Analysis,” 2025.

[7] N. Hosseinzadeh *et al.*, “Concrete Seawalls: Load Considerations, Ecological Performance, Durability, and Recent Innovations,” 2021.

[8] R. K. Gittman, S. B. Scyphers, C. S. Smith, I. P. Neylan, and J. H. Grabowski, “Ecological consequences of shoreline hardening: a meta-analysis,” *BioScience*, vol. 66, no. 9, pp. 763–773, 2016.

[9] S. M. R. Ghiasian, “Structural Morphogenesis of Green/Gray Coastal Infrastructure: Paradigms for Shoreline Protection,” 2022.

[10] A. Harasti, G. Gilja, K. Potočki, and M. Lacko, “Scour at bridge piers protected by the riprap sloping structure: A review,” *Water*, vol. 13, no. 24, p. 3606, 2021.

[11] P. F. Lagasse, *Countermeasures to protect bridge piers from scour*, vol. 593. Transportation Research Board, 2007.

[12] K. Wardhana and F. C. Hadipriono, “Analysis of recent bridge failures in the United States,” *Journal of performance of constructed facilities*, vol. 17, no. 3, pp. 144–150, 2003.

[13] B. Aykac, I. Kalkan, S. Aykac, and Y. E. Egriboz, “Flexural behavior of RC beams with regular square or circular web openings,” *Engineering Structures*, vol. 56, pp. 2165–2174, 2013.

[14] S. Aykac and M. Yilmaz, “Behaviour and strength of RC beams with regular triangular or circular web openings,” *Journal of the Faculty of Engineering and Architecture of Gazi University*, vol. 26, no. 3, 2011.

[15] S. A. Al-Sheikh, “Flexural behavior of RC beams with opening,” *Concrete Research Letters*, vol. 5, no. 2, pp. 812–824, 2014.

[16] J. Daniel and J. Revathy, “Experimental investigation on flexural strength of beams with opening,” *Int J Res Manage Tech (IJRMT)*, vol. 4, no. 2, pp. 141–143, 2014.

[17] K.-H. Tan and M. A. Mansur, “Design procedure for reinforced concrete beams with large web openings,” *Structural Journal*, vol. 93, no. 4, pp. 404–411, 1996.

[18] S. Amiri, R. Masoudnia, and M. A. Ameri, “A review of design specifications of opening in the web for simply supported RC beams,” *J. Civ. Eng. Constr. Technol*, vol. 2, no. 4, pp. 82–89, 2011.

[19] M. Mansur and K.-H. Tan, *Concrete beams with openings: analysis and design*, vol. 20. CRC Press, 1999.

[20] American Concrete Institute (ACI), *Building Code Requirements for Structural Concrete (ACI 318-19) and Commentary*. Farmington Hills, MI: American Concrete Institute, 2019.

[21] C. C. Steputat, S. Nolan, L. Denty, P. A. Kaminski, and A. Nanni, “A seawall constructed with GFRP bars as structural reinforcing,” *Concrete International*, vol. 41, no. 9, pp. 26–30, 2019.

[22] C. Yang, L. Li, and J. Li, “Service life of reinforced concrete seawalls suffering from chloride attack: Theoretical modelling and analysis,” *Construction and Building Materials*, vol. 263, p. 120172, 2020.

[23] ACI PRC-440.1-15, “Guide for the design and construction of structural concrete reinforced with fiber-reinforced polymer FRP bars,” *American Concrete Institute*, 2015.

[24] CSA_S806-12, “Design and construction of building structures with fibre-reinforced polymers,” 2021.

[25] L. R. Taerwe, H. Lambotte, and H.-J. Miesseler, “Loading tests on concrete beams prestressed with glass fiber tendons,” *PCI Journal*, vol. 35, no. 4, 1992.

[26] M. Balah and S. Abdel-Mawla, “Efficiency of permeable caisson seawall reinforced with fibre reinforced polymers,” presented at the Composite Materials in Concrete Construction: Proceedings of the International Seminar held at the University of Dundee, Scotland, UK on 5–6 September 2002, Thomas Telford Publishing, 2002, pp. 265–275.

[27] ACI Committee 440, “Building Code Requirements for Structural Concrete Reinforced with Glass Fiber-Reinforced Polymer (GFRP) Bars - Code and Commentary (ACI CODE-440.11-22),” *American Concrete Institute, Farmington Hills, MI*, 2023.

[28] B. Standard, “Testing hardened concrete,” *Compressive strength of test specimens, BS EN*, pp. 12390–3, 2009.

[29] M. Rossini, “FRP reinforcement for prestressed concrete applications,” 2019.

[30] ASTM D7957/D7957M-22, *Standard Specification for Solid Round Glass Fiber Reinforced Polymer Bars for Concrete Reinforcement*. ASTM International, 2022.

[31] S. Narayanan, “Effect of Size and Shape of Test Specimen on Compressive Strength of Concrete.,” *Concrete International*, vol. 46, no. 1, 2024.

[32] H. Ju, M. Yerzhanov, D. Lee, H. Shin, and T. H.-K. Kang, “Modifications to ACI 318 shear design method for prestressed concrete members: Detailed method.,” *PCI Journal*, vol. 68, no. 1, 2023.

[33] Y. J. Kim, “Mitigation of End Zone Cracking in Prestressed Concrete Girders,” Colorado Department of Transportation. Applied Research & Innovations Branch, 2024.